Author's Version

Microplasticity and macroplasticity behavior of additively manufactured Al-Mg-Sc-Zr alloys: In-situ experiment and modeling

X.X. Zhang[1,2,*], P.-P. Bauer[3], A. Lutz[4], C. Wielenberg[5], F. Palm[6], W.M Gan[7], E. Maawad[7]

[1] Institute of High Energy Physics, Chinese Academy of Sciences, Beijing 100049, People's Republic of China.

[2] Heinz Maier-Leibnitz Zentrum (MLZ), Technische Universität München, Lichtenbergstr. 1, 85748 Garching, Germany

[3] German Aerospace Center (DLR), Institute of Materials Research, Linder Hoehe, D-51147 Cologne, Germany

[4] Mercedes Benz AG, Research and Development Department, Leibnizstr. 2, 71032 Böblingen, Germany

[5] Premium AEROTEC GmbH, Riesweg 151-155, 26316 Varel, Germany

[6] Airbus Central Research & Technology (CRT), Airbus Defence and Space GmbH, Willy-Messerschmitt-Str. 1, 82024 Taufkirchen, Germany

[7] Institute of Materials Physics, Helmholtz-Zentrum Hereon, Max-Planck-Str. 1, 21502 Geesthacht, Germany

International Journal of Plasticity (2023)

https://doi.org/10.1016/j.ijplas.2023.103659

Microplasticity and macroplasticity behavior of additively manufactured Al-Mg-Sc-Zr alloys: in-situ experiment and modeling

X.X. Zhang[1,2,*], P.-P. Bauer[3], A. Lutz[4], C. Wielenberg[5], F. Palm[6], W.M Gan[7], E. Maawad[7]

[1] Institute of High Energy Physics, Chinese Academy of Sciences, Beijing 100049, People's Republic of China.

[2] Heinz Maier-Leibnitz Zentrum (MLZ), Technische Universität München, Lichtenbergstr. 1, 85748 Garching, Germany

[3] German Aerospace Center (DLR), Institute of Materials Research, Linder Hoehe, D-51147 Cologne, Germany

[4] Mercedes Benz AG, Research and Development Department, Leibnizstr. 2, 71032 Böblingen, Germany

[5] Premium AEROTEC GmbH, Riesweg 151-155, 26316 Varel, Germany

[6] Airbus Central Research & Technology (CRT), Airbus Defence and Space GmbH, Willy-Messerschmitt-Str. 1, 82024 Taufkirchen, Germany

[7] Institute of Materials Physics, Helmholtz-Zentrum Hereon, Max-Planck-Str. 1, 21502 Geesthacht, Germany

Abstract

Understanding and controlling the performance of additively manufactured aluminum alloys containing scandium (Sc) and zirconium (Zr) elements heavily relies on knowledge of their microplasticity and macroplasticity behavior. However, this aspect has received very little attention. In this investigation, we examined the microplasticity and macroplasticity behavior of additively manufactured Al-Mg-Sc-Zr

*Corresponding author. E-mail address: xxzhang@ihep.ac.cn (X.X. Zhang)

alloys before and after aging, using in-situ synchrotron X-ray diffraction and full-field crystal plasticity modeling. Our study provides a quantitative assessment of the transitions from elasticity to microplasticity and then to macroplasticity and analyzes the development of the initial microstructure, particularly the dislocations. We constructed crystal plasticity fast-Fourier-transform models based on dislocation densities. The predicted evolutions of macroscopic stress-strain curves, lattice strains, and dislocation densities agree with in-situ measurements. The present findings provide deep insights into controlling the performance of AM Al-Mg-Sc-Zr alloys. Besides, the micromechanical model developed in this investigation paves the way for predicting the microplasticity and macroplasticity behavior of various metallic materials.

Keywords: Aluminum alloy; additive manufacturing; synchrotron X-ray diffraction; microplasticity; dislocation density; strain hardening mechanism; crystal plasticity

1. Introduction

The use of scandium (Sc) and zirconium (Zr) as alloying elements has attracted considerable attention in developing high-performance aluminum alloys for additive manufacturing (AM) over the last decade. One such example is Scalmalloy®, an Al-Mg-Sc-Zr alloy developed by (Schmidtke et al., 2011), which was the first AM-oriented Al alloy exhibiting high strength, fatigue and toughness properties, and corrosion resistance (Herzog et al., 2016; Schmidtke, 2020; Spierings et al., 2017; Spierings et al., 2016). Subsequently, several other Al-*x*-Sc-Zr alloys have been developed for AM (Bayoumy et al., 2022; Jia et al., 2019b; Li et al., 2020a).

The relationships between the alloying composition, microstructure, and mechanical properties were extensively studied for these new AM Al alloys (Jia et al., 2019a; Jia et al., 2019b; Li et al., 2020a;

Spierings et al., 2018a; Spierings et al., 2017; Wang et al., 2021a). The effects of AM conditions, such as scan strategy (Li et al., 2017; Spierings et al., 2016), laser parameters (Li et al., 2017; Schmidtke et al., 2011; Shi et al., 2017; Spierings et al., 2016), and preheating temperature of the substrate (Shi et al., 2018), and heat treatment (Khomutov et al., 2021; Li et al., 2020a; Wang et al., 2021b) on the microstructure and properties of these new alloys were thoroughly investigated. However, very little attention has been paid to their microplasticity and macroplasticity behavior.

Microplasticity refers to the plastic activity at small strains before macroscopic yielding. The boundary between microplasticity and macroplasticity is commonly defined using a practical concept - the 0.2% offset yield stress (Li and Wagoner, 2021; Maaß and Derlet, 2018; Zhu and Wu, 2023). Investigating microplasticity is essential. Practically, microplastic information is valuable in selecting materials for purely elastic and high dimensional-stability applications. This is especially important for AM components, which often have topology-optimized and intricate geometry and are in a non-equilibrium state. Therefore, accurately maintaining their geometry and microstructure during service is crucial for high-value AM applications. Fundamentally, microplasticity accounts for the transition from elastic to plastic activity. It is known that before macroscopic yielding, microplasticity deformation has already occurred (Berger et al., 2022). However, there are still many unanswered questions regarding microplasticity deformation (Arechabaleta et al., 2016; Li and Wagoner, 2021; Maaß and Derlet, 2018). For example, how does the initial microstructure, particularly the dislocations, evolve from elasticity to macroplasticity? What is the relationship between dislocation density, plastic strain, and stress during microplasticity deformation? This relationship in the microplasticity stage is complex and often poorly understood (Maaß and Derlet, 2018).

After the microplasticity stage, the material enters the macroplasticity stage, where the majority of grains undergo plastic deformation with significant dislocation activities (Beyerlein and Tome, 2008; Chen et al., 2021b). This stage is closely linked to strain hardening behavior and elongation, which are critical for various engineering applications. The development of dislocation structures and accumulation of dislocations during the macroplasticity stage contribute to strain hardening (Wei et al., 2022). In order to comprehend strain hardening behavior and elongation, it is essential to investigate the dislocations, as they are the primary carriers of plastic deformation in metals, and their behavior directly affects the mechanical properties of the material. In the case of the AM Al-*x*-Sc-Zr alloys, direct aging is typically required to increase strength through precipitation strengthening (Cordova et al., 2020; Herzog et al., 2016; Li et al., 2020a). This raises important questions: How does direct-aging treatment affect macroplasticity behavior? What are the micromechanical aspects that contribute to changes in macroplasticity behavior before and after direct aging? How does the dislocation behavior change before and after direct aging? Answering these questions is crucial to control the performance of AM Al-*x*-Sc-Zr alloys.

In this study, we investigated the microplasticity and macroplasticity behavior of additively manufactured Al-Mg-Sc-Zr alloys before and after aging using in-situ synchrotron X-ray diffraction (SXRD) and full-field crystal plasticity modeling. The bulk textures before and after aging were measured using SXRD. The microstructures were analyzed using optical microscopy (OM) and electron backscatter diffraction (EBSD). Crystal plasticity fast-Fourier-transform (CPFFT) models based on dislocation densities were constructed and validated. Quantitative assessments of the transitions from elasticity to microplasticity and then to macroplasticity were performed, and the development of the initial microstructure, particularly the dislocations, was analyzed in detail. Our findings provide valuable insights into the underlying mechanisms responsible for the microplasticity and macroplasticity behavior of AM Al-Mg-Sc-Zr alloys. Furthermore, the micromechanical models developed here can be extended to predict the micromechanical behavior of other metallic materials.

2. Experimental procedure

2.1 Additive manufacturing and heat treatment

The Scalmalloy® specimens were manufactured using the laser powder bed fusion (LPBF) method. Toyal Europe Company supplied the Scalmalloy® powder, which had a size distribution of d_{10}=31.9 µm, d_{50}=47.0 µm, and d_{90}=68.4 µm. The chemical composition of the powder is Al-4.7Mg-0.78Sc-0.29Zr-0.48Mn-0.10Fe-0.07Si (wt.%). The specimens were built vertically using an EOS M290 system, with a laser power of 370 W, a laser scan speed of 1275 mm/s, and a volume energy density of 64.48 J/mm^3 under an argon gas atmosphere. Direct aging treatment was applied under 325 °C for 4 hours in a circulating air oven, followed by water-quenching. The AM specimens were near-net-shaped, and the as-built and direct-aged specimens were machined to remove surface defects, resulting in dog-bone-shaped round tensile specimens. The removed surface layer of the parallel part was approximately 0.5 mm thick. The final diameter and length of the parallel part of the tensile specimens were 4 and 30 mm, respectively.

2.2 Optical microscopy analysis

Optical image characterization was performed to analyze the size and distribution of pores and other defects on a reflected-light microscope of the type ZEISS Axio Imager.M2m. Images were captured on 10×10×10 mm^3 cubes (ground and polished) in a centered position with a direction normal to the XY plane. These cubes were manufactured in the same printing job to ensure consistency.

2.3 Electron backscatter diffraction analysis (EBSD)

The EBSD analysis was conducted using a Zeiss Ultra 55 scanning electron microscope equipped with an Oxford Nordlys II EBSD detector. The samples were cut along the Z direction and polished manually. Then, the samples were electrolytically polished. High-resolution mapping was performed with a step size of 30 nm/step, resulting in an acquisition time of approximately 60 hours for the high-resolution images. The zero solutions were removed by matching them to indexed, adjacent pixels. The number of nearest neighbors with a solution was stepwise reduced from 8 to 4 until zero solutions were removed. Finally, any wild spikes up to 2 pixels in size were removed.

2.4 In-situ synchrotron X-ray diffraction

The in-situ SXRD experiment was performed at the High Energy Materials Science (HEMS) beamline P07B of the Helmholtz-Zentrum Hereon at PETRA III, DESY. The specimens were subjected to tensile loading using a tensile rig placed on the sample table. The crosshead displacement speed was maintained at 0.36 mm/min, which corresponded to a nominal strain rate of 3.0×10^{-4} s^{-1}.

An Instron 2620-602 extensometer and a Kyowa KFEM-2-120-C1L1M2R high-accuracy strain gauge were utilized to measure strain simultaneously. The strain gauge was attached to the side of the X-ray incident location. Therefore, the average strain within the extensometer, which had an initial distance of 12.5 mm, and the precise local strain at the X-ray incident location were recorded simultaneously. Fig. 1(a) provides an overview of the experimental setup, and Fig. 1(b) displays the tensile specimen with the extensometer and the strain gauge.

The initial bulk textures of the as-built and direct-aged specimens were measured before loading using the SXRD, without the tensile rig but with a rotation sample table. The sample table rotates around the longitudinal axis of the specimens from -90° to 90° with a step size of 5° for texture measurements.

The synchrotron X-ray had a wavelength of 0.14235 Å and a spot size of 0.7×0.7 mm^2. A two-dimensional PerkinElmer XRD 1622 detector with a pixel size of 200×200 μm^2 and 2048×2048 pixels was used to record the diffraction patterns.

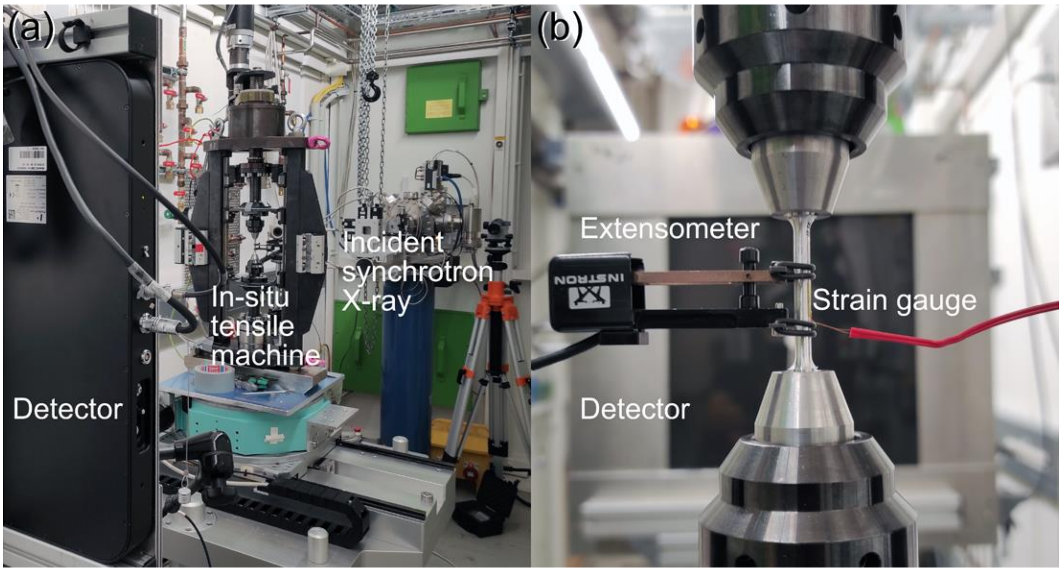

Fig. 1 In-situ SXRD experiment setup at the beamline P07B, DESY: (a) an overview; (b) a close view of the tensile specimen, extensometer, and strain gauge. The X-ray incident location is at the center between the two arms of the extensometer, and the strain gauge is on the side of the X-ray incident location.

2.5 Calculations of lattice strain and diffraction elastic constants

The 10° cake segments of the 2D diffraction images at the positions of 0°±5° and 180°±5° were used to calculate the diffraction spectrums for the transversal direction (TD). Those at the positions of 90°±5° and 270°±5° were used to calculate the diffraction spectrums for the loading direction (LD). The {*hkl*} lattice strain ε_{hkl}^{s} in the direction *s* (*s* = LD or TD) is calculated by

$$\varepsilon_{hkl}^{s} = \frac{\sin\theta_{hkl,0}^{s}}{\sin\theta_{hkl}^{s}} - 1, \tag{1}$$

where θ is the peak position, and subscript 0 denotes the reference condition before loading. No Einstein summation on *s* or *hkl* exists.

The {*hkl*} elastic moduli E_{hkl} can be determined by

$$E_{hkl} = \frac{\partial\sigma_{\mathrm{LD}}}{\partial\varepsilon_{hkl}^{\mathrm{LD}}}, \tag{2}$$

where σ_{LD} is the applied stress, $\varepsilon_{hkl}^{\mathrm{LD}}$ the lattice strain in the LD.

For materials with weak textures, the {*hkl*} Poisson's ratio ν_{hkl} can be calculated by

$$\nu_{hkl} = -\frac{\partial \varepsilon_{hkl}^{\mathrm{TD}}}{\partial \varepsilon_{hkl}^{\mathrm{LD}}}. \tag{3}$$

2.6 Determination of dislocation density through line profile analysis

The modified Williamson-Hall (mWH) method (Ungar and Borbely, 1996) was used to assess dislocation density evolution during loading qualitatively. However, this method has limitations in accurately separating instrumental and size contributions, and it describes the size and strain effects using simplified functions and parameters, resulting in relatively large errors (Scardi and Leoni, 2006; Scardi et al., 2004). To obtain more reliable results, the convolutional multiple whole profile (CMWP) procedure (Ribarik et al., 2019; Ribarik and Ungar, 2010) was also adopted to determine the dislocation density. The physical profile is broadened by (i) size broadening due to small coherently scattering domains and (ii) strain broadening that is produced by dislocations and is described by the mean square strain $\langle \varepsilon^2 \rangle$. In the CMWP procedure, the physical profile functions are obtained by convolution of the theoretical size and strain profile functions. The mean square strain $\langle \varepsilon^2 \rangle$ is calculated by

$$\langle \varepsilon^2 \rangle = \frac{\rho \bar{C} b}{4\pi} f(\eta), \tag{4}$$

where ρ is the dislocation density, $\bar{C}$ and *b* are the contrast factor and Burgers vector of dislocations, and $f(\eta)$ is the Wilkens function (Ribarik and Ungar, 2010).

3. Results

3.1 Macroscopic mechanical properties

Fig. 2 shows the engineering stress, strain from the extensometer, and strain from the strain gauge as functions of time. After yielding, the strain development with time is stepwise for both as-built and direct-aged specimens, indicating that plastic deformation is localized in both materials (Benallal et al., 2008). In contrast, during homogeneous plastic deformation, the strain magnitude increases continuously and smoothly with time (Zhang et al., 2021a). As both materials exhibit localized plastic deformation, it is expected that the strain measured by the strain gauge differs from that of the extensometer. Specifically, the strain gauge measures the local strain experienced at the synchrotron X-ray incident location, while the extensometer provides the average strain within the two arms of the extensometer (see Fig. 1(b)).

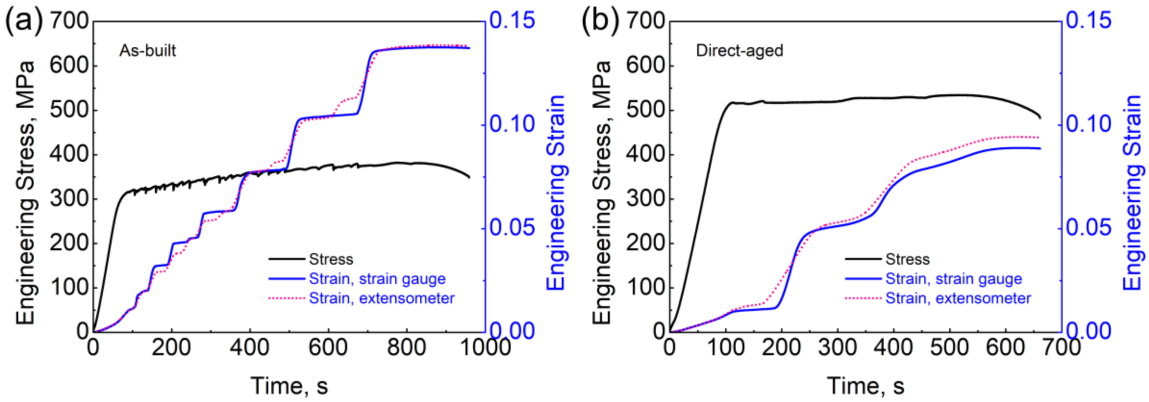

Fig. 2 Evolutions of engineering stress, engineering strain measured from extensometer, and engineering strain measured from strain gauge with time for the (a) as-built and (b) direct-aged specimens.

The stress-strain curves for the as-built and direct-aged specimens are presented in Fig. 3(a). Prior to macroscopic yielding, the stress-strain curve based on the strain gauge coincides with that based on the extensometer. In Fig. 3(b), the stress-strain curve for the as-built material deviates from linearity at a stress of 113.7 MPa, which is the proportional limit σ_{PL} . The σ_{PL} value for the direct-aged material is 407.2 MPa. Additionally, the yield strength $\sigma_{0.2}$ for the as-built and direct-aged materials is 293.6 MPa and 513.0 MPa, respectively (Fig. 3(b)). Therefore, the direct-aging treatment significantly increases both the proportional limit and yield strength.

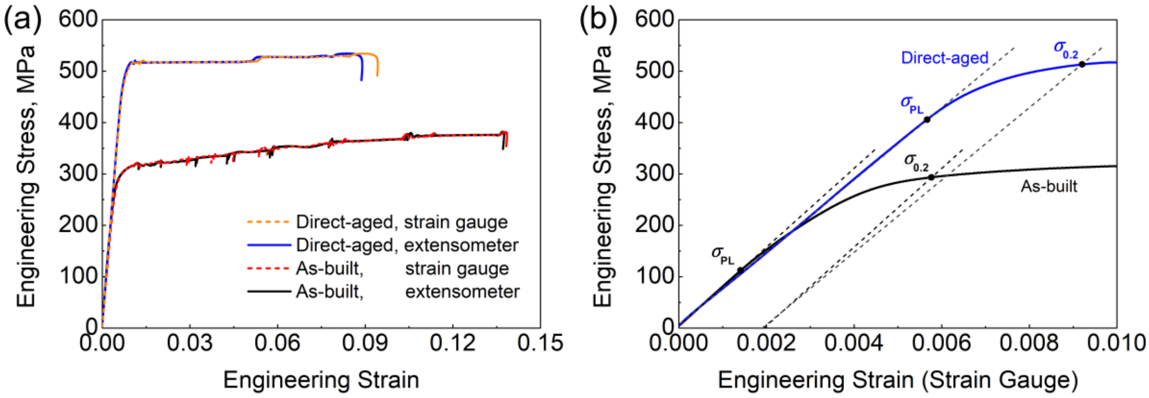

Fig. 3 Stress-strain curves of the as-built and direct-aged specimens: (a) engineering stress-strain curves. The strains measured from both the strain gauge and extensometer are compared here. (b) Engineering stress-strain curves in the small strain range.

It is noteworthy that both specimens exhibit serrations in their stress-strain curves during macroplasticity, as shown in Fig. 3(a). These serrations are attributed to the Portevin-Le Chatelier (PLC) effect. This effect is often observed in solute-strengthened alloys, such as the Al-Mg alloys, and results in unstable plastic flow and a serrated stress-strain curve (Chen et al., 2021a, b). The PLC effect is associated with dynamic strain aging (DSA), which is attributed to the interactions between diffusive solute atoms (e.g., Mg atoms) and mobile dislocations (Curtin et al., 2006). Previous research (Rodriguez, 1984; Zhang et al., 2017) has shown that the serrations caused by the PLC effect can be classified into different categories: types A, B, C, D, and E. Type A serrations show an abrupt rise followed by a drop, which is caused by the dislocation locking mechanism. Type B serrations are oscillations around the average level of the stress-strain curve, usually developed from type A with increasing strain. Type C serrations are stress drops below the average level of the stress-strain curve, which are associated with the dislocation unlocking mechanism. Type D serrations show plateaus in the stress-strain curve with no obvious strain hardening. Type E serrations often appear at high strains, similar to type A but with little or no strain hardening (Rodriguez, 1984). Based on these definitions, different types of serrations for both specimens are marked in Figs. 4(a) and (b).

The PLC behavior causes local variations in the strain rate. In the present in-situ tensile experiments, a constant nominal strain rate of 3.0×10^{-4} s^{-1} was used (with a crosshead displacement speed of 0.36 mm/min). However, the recorded true strain rate values for the as-built material varied between -1×10^{-3} and 3×10^{-3} s^{-1} (Fig. 4(c)), while that of the direct-aged material varied between 0 and 1.5×10^{-3} s^{-1} (Fig. 4(d)). Despite these instantaneous fluctuations, the magnitudes of the true strain rates remained very low and within the quasi-static condition. Therefore, the effect of the instantaneous strain rate on the mechanical properties is expected to be small.

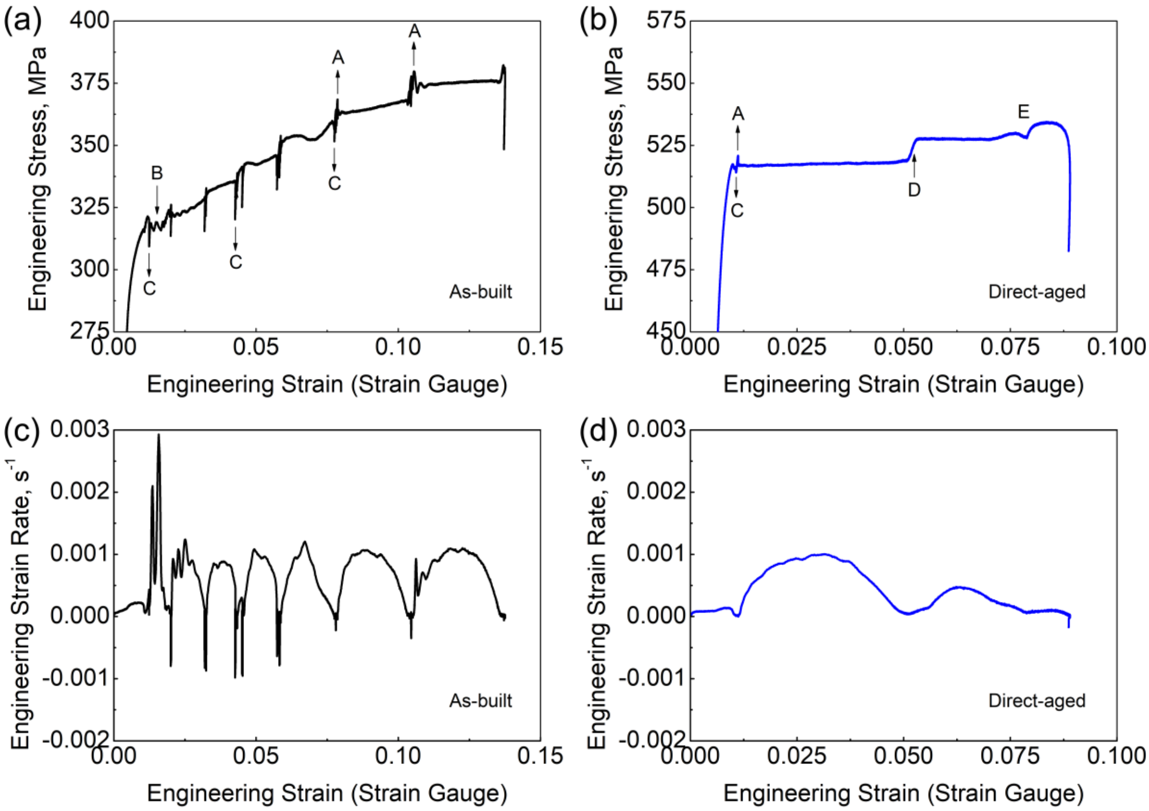

Fig. 4 Detailed stress-strain curves and the corresponding strain rate evolutions.

3.2 Porosity

Fig. 5(a) presents a typical OM image at 12.5× magnification, which provides an overview of the pores in the as-built specimen. To capture more fine pores, we used 11 OM images at 25× magnification to measure the porosity in the as-built specimen. However, pores with diameters smaller than one pixel, which denotes 2.88 μm at this magnification, could not be analyzed. The determined porosity of the as-built specimen is 0.44±0.07%, which is consistent with previous reports (Spierings et al., 2017; Spierings et al., 2018b). Fig. 5(b) presents a detailed statistical analysis of the pores. The minimum, maximum, and average pore diameters are 10.44, 140.73, and 18.29 μm, respectively. Moreover, 91.57% of the pores have diameters smaller than 30 μm, and most of the pores are round, indicating that the metallurgical pores dominate the pore population (Aboulkhair et al., 2014).

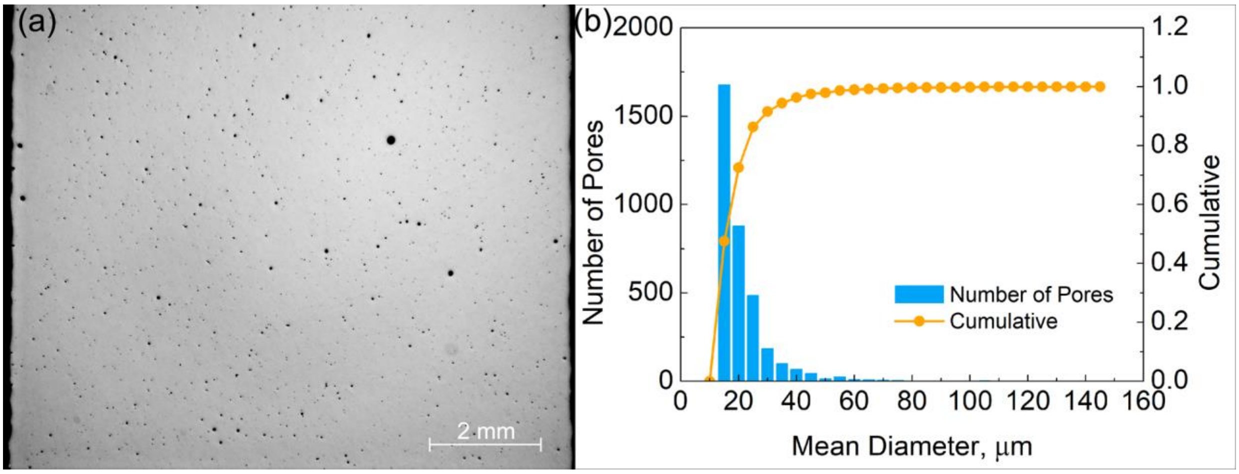

Fig. 5 OM microstructure: (a) a typical optical microscopy image shows an overview of the pores in the as-built specimen; (b) statistics of pores.

3.3 Bulk texture

The gauge volume used for the texture measurements via SXRD was 0.7×0.7×4 mm^3. Meanwhile, the sample rotated during texture measurements. Hence, the measured textures reflect averaged properties.

The peak intensity pole figures of the as-built and direct-aged materials are shown in Fig. 6. The 200 pole figure indicates a typical <001>//Z fiber texture in both materials, with the maximum intensity value of this fiber texture being only 1.29 and 1.25 multiples of a random density (MRD) in the as-built and direct-aged materials, respectively. These results indicate that the bulk textures in both materials are weak, and the direct-aging treatment has only a minimal effect on the texture.

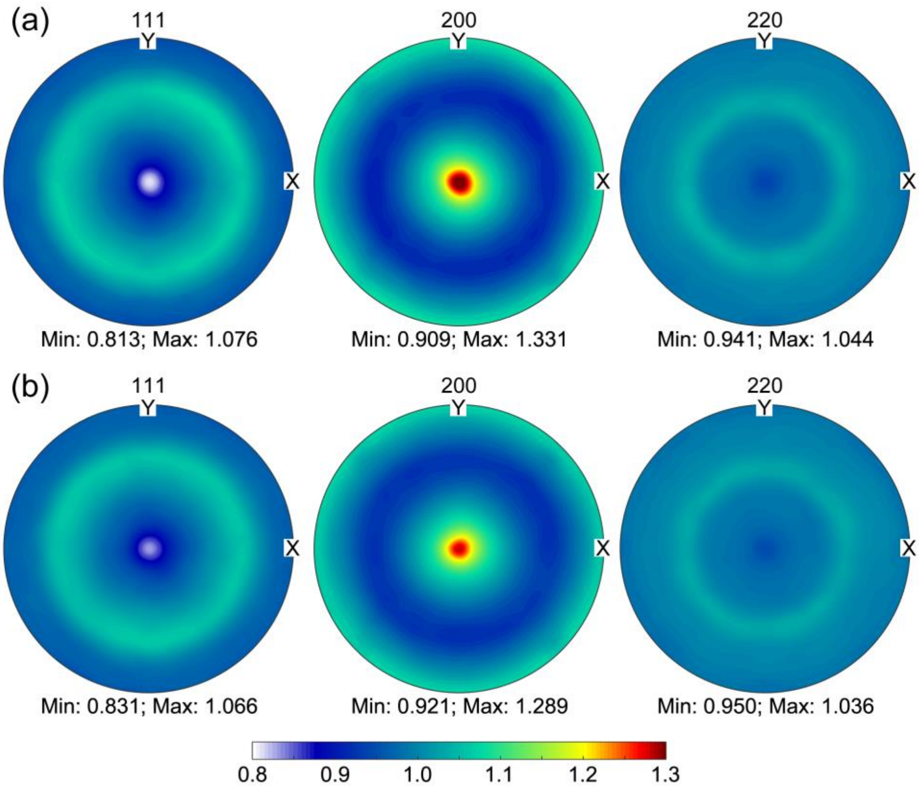

Fig. 6 Peak intensity pole figures of the (a) as-built and (b) direct-aged specimens prior to loading. The Z direction is parallel to the building direction. The X and Y directions are parallel to the base plate.

The full width at half maximum (FWHM) pole figures shown in Fig. 7 reveal two main features. Firstly, both materials exhibit a fiber texture, with grain families oriented parallel to the Z direction having smaller FWHM values. This suggests that these grain families experienced less plastic deformation during the AM process, while those with crystallographic orientations parallel to the base plate show larger

FWHM values, indicating greater plastic deformation caused by inhomogeneous thermo-mechanical deformation (Xie et al., 2020). Secondly, the FWHM values of the direct-aged material are lower than those of the as-built material. This is attributed to the thermal annealing effect caused by the aging process, which reduces the dislocation density in the direct-aged material.

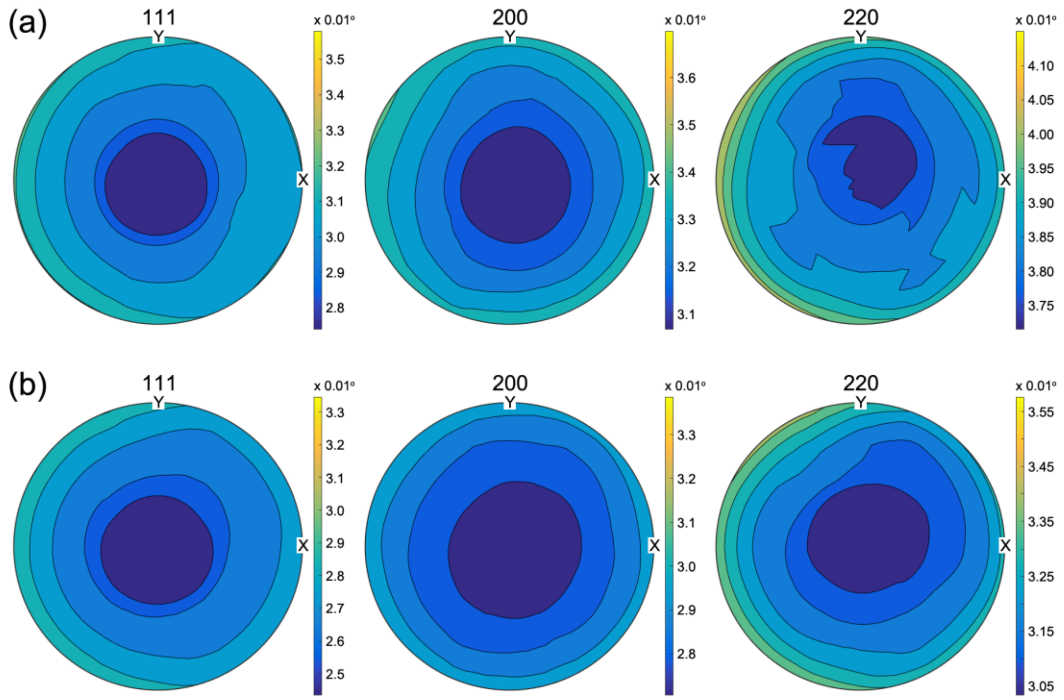

Fig. 7 FWHM pole figures of the (a) as-built and (b) direct-aged specimens prior to loading. The definitions of X, Y, and Z directions are the same as those in Fig. 6.

3.4 Microstructure

It has been reported that the as-built Scalmalloy® alloy consists of a bimodal grain structure. The coarse grains have a grain size ranging from ~2 to ~13 μm and show a typical <001>//Z fiber texture. Fine grains have a grain size ranging from ~0.15 μm to ~2 μm, depending on the manufacturing conditions, and display random grain orientations (Spierings et al., 2016). According to simulations and detailed transmission electron microscopy (TEM) characterizations, the fine grains are formed due to the high number density of seed crystals, including $Al_3(Sc, Zr)$ and mixed oxide particles (Al-Mg-oxides) around the melt-pool boundary, which stimulate simultaneous growth of fine grains. The coarse columnar grains, on the other hand, are associated with the high-temperature gradient and low number density of seed crystals (Al-Mg-oxides) (Spierings et al., 2017; Spierings et al., 2018b). It is worth noting that the grain structure of the as-built Scalmalloy® alloy demonstrates excellent thermal stability as the grain boundaries are pinned by small $Al_3(Sc, Zr)$ particles (Spierings et al., 2017).

A significant amount of Sc and Zr remains in the solid solution due to the high cooling rates during LPBF processing. During the direct aging treatment, $Al_3(Sc, Zr)$ particles form. For instance, based on atom probe tomography (APT) analysis, (Spierings et al., 2018a) showed that the direct aging at 325 °C for 4 hours increases the $Al_3(Sc, Zr)$ particle number density in the Scalmalloy® alloy from 0.5-1.0×10^{23} m^{-3} (as-built) to 5.2×10^{23} m^{-3} (direct-aged). The $Al_3(Sc, Zr)$ particle number density in the direct-aged state increases by a factor of about 3-10 compared to the as-built state. These $Al_3(Sc, Zr)$ particles typically have sizes ≤ 5 nm. This APT analysis also revealed that the direct aging treatment at 325 °C for 4 hours is sufficient to precipitate almost all Sc to form Al_3Sc or $Al_3(Sc, Zr)$ particles (Spierings et al., 2018a).

The present EBSD images of both specimens in Figs. 8(a) and (b) confirm the previously reported bimodal grain structure (Cordova et al., 2020; Schimbäck et al., 2022; Spierings et al., 2018a; Spierings et al., 2017; Spierings et al., 2018b; Spierings et al., 2016). The fine grains in the as-built specimen have circle equivalent grain diameters ranging from ~0.1 to ~2.0 μm, while those of the coarse grains range from ~2.0 to ~14.0 μm (Fig. 8(a)). The lognormal mean grain sizes of the as-built and direct-aged specimens are 0.78±0.59 and 0.83±0.54 μm, respectively, indicating that the grain size remains almost the same after aging. The 111, 200, and 220 pole figures of both specimens obtained from the EBSD images exhibit similar patterns to those obtained from the SXRD (Fig. 6), but with different pole figure intensities.

The maximum intensity values of the local <001>//Z fiber texture at the microscale in the as-built and direct-aged specimens are about 4.10 and 4.89 MRD, respectively, which are about 3.2-3.9 times those determined from bulk textures (Figs. 8(c) and (d)).

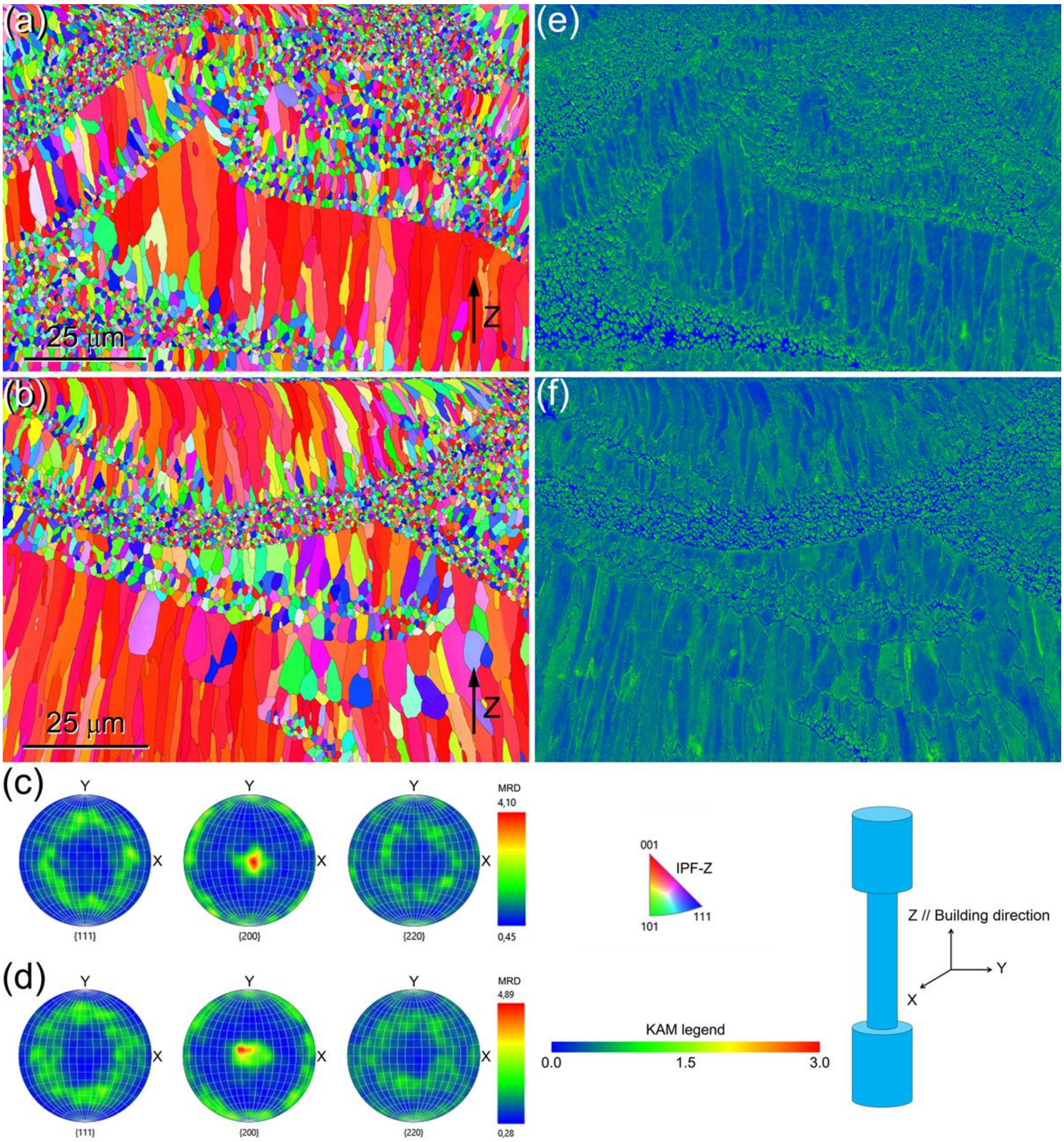

Fig. 8 EBSD microstructures before tensile deformation: IPF maps of (a) the as-built and (b) direct-aged specimens; pole figures of the (c) as-built and (d) direct-aged specimens; KAM maps of (a) the as-built and (b) direct-aged specimens. The legends of the IPF map and KAM map are shown in the bottom right corner, as well as the definition of the sample coordinate system.

The KAM maps presented in Figs. 8(e) and (f) illustrate the local strains resulting from the accumulation of geometrically necessary dislocations. Both specimens exhibit relatively high KAM values of about 1.5º. In the as-built specimen, the fine grains in the up region show a slightly more intensive distribution of high KAM values due to a large number of grain boundaries than the coarse grains. The fine grains in the bottom region of Fig. 8(e) and in the middle region of Fig. 8(f) show more blue colors, which is due to the data cleaning process. Figs. 8(e) and (f) show that there is no significant difference in the KAM maps between the as-built and direct-aged specimens.

3.5 Evolutions of lattice strains

Fig. 9 displays the SXRD spectrums of the as-built and direct-aged specimens before loading. In both materials, only Al peaks can be detected. For the direct-aged material, the $Al_3(Sc, Zr)$ precipitates have the $L1_2$ crystal structure and are completely coherent with the Al matrix (Li et al., 2014). When the materials are subjected to tensile loading, the distances between various {*hkl*} lattice planes alter, causing diffraction peaks to shift.

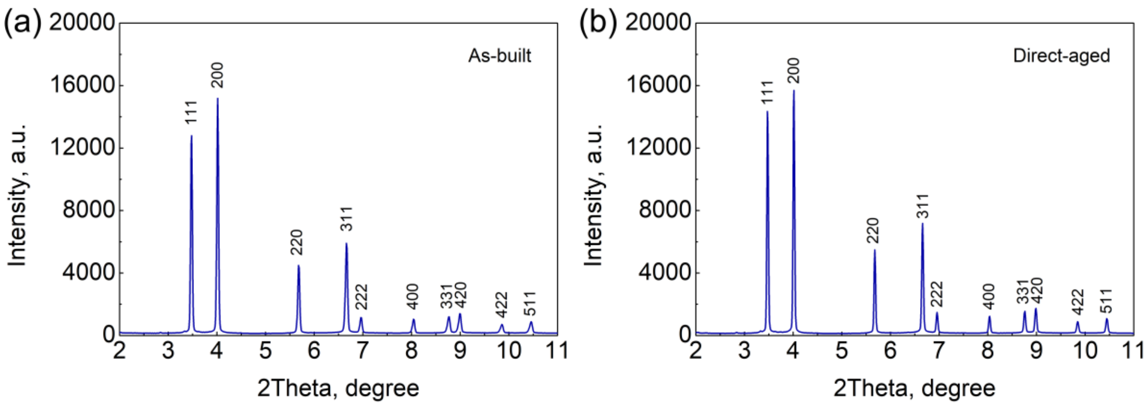

Fig. 9 SXRD spectrums of the (a) as-built and (b) direct-aged specimens prior to loading.

From peak shifting, the {*hkl*} lattice strains in the LD and TD of both materials are calculated using Eq. (1), as shown in Fig. 10. For the as-built material (Fig. 10(a)), the lattice strain vs. applied true stress curves can be divided into four zones based on their evolutions: rA (elasticity, until σ_{PL}), rB1 (microplasticity stage 1, until 276.9 MPa due to dislocation behavior), rB2 (microplasticity stage 2, until 324.7 MPa), and rC (macroplasticity, until fracture) zones. In the elasticity stage, all lattice strains in both LD and TD vary linearly with the applied true stress. In the microplasticity stage 1, the lattice strain vs. applied true stress curves exhibit slight deviations from elastic slopes due to a small amount of plastic deformation. In the microplasticity stage 2, the {200} lattice strain curve in the TD shows more pronounced nonlinearity due to increased intergranular strains. Further details about the microplasticity stages, which are associated with dislocation behavior, are explained in section 3.6.

In the macroplasticity stage, a wider spread of {*hkl*} lattice strains is observed, indicating that plastic deformation becomes more heterogeneous. In texture-free FCC metals, the {311} lattice strain is approximately linear with applied stress in both LD and TD (Clausen et al., 1998). However, during the macroplasticity stage, the {311} lattice strain of the as-built specimen is nonlinear in the LD but linear in the TD (see Fig. 10(a)). This inconsistency is likely caused by texture effects, which reduce particular grain statistics due to preferred grain orientations (Choo et al., 2020; Schroeder et al., 2021). Another possibility is that the nonlinear evolution of {311} lattice strain could also be caused by anisotropic residual strains within the as-built sample, as suggested by (Wang et al., 2018).

The evolutions of lattice strains in the direct-aged material can also be divided into four zones (Fig. 10(b)): rA (elasticity, until σ_{PL}), rB (microplasticity, until 522.4 MPa), rC1 (macroplasticity stage 1, separated due to dislocation behavior), and rC2 (macroplasticity stage 2, until fracture) zones. The macroplasticity stage is divided into two sub-stages that are associated with the dislocation behavior and will be explained in section 3.6. It is noteworthy that the {311} lattice strain curves in both LD and TD are linear with the applied true stress for the direct-aged material.

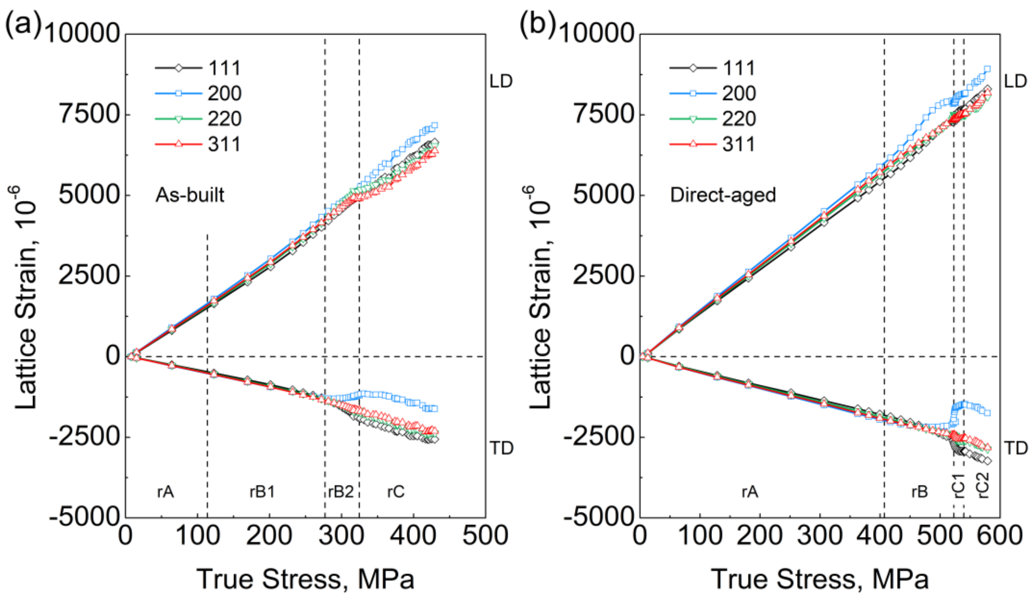

Fig. 10 Evolutions of different *hkl* lattice strains with applied true stress in both LD and TD for the (a) as-built and (b) direct-aged specimens. For both LD and TD, the maximum lattice strain error of the as-built specimen is smaller than 76×10^{-6}, and that of the direct-aged specimen is smaller than 60×10^{-6}.

Table 2 Experimental and Kröner model (Zhang et al., 2021b) predicted diffraction elastic constants of the as-built and direct-aged specimens.

hkl	Elastic moduli E_{hkl}			Poisson's ratio ν_{hkl}		
	As-built	Direct-aged	Kröner model	As-built	Direct-aged	Kröner model
111	70.21	72.88	73.09	0.309	0.327	0.342
200	64.49	67.12	67.44	0.318	0.329	0.354
220	68.38	70.09	71.59	0.320	0.327	0.345
311	66.92	69.14	69.99	0.321	0.332	0.348

The evolutions of lattice strains can be used to determine the {*hkl*} diffraction elastic constants and Poisson's ratio using Eqs. (2)-(3), as summarized in Table 2. For comparison, the Kröner model predictions based on a random texture assumption are also listed (Zhang et al., 2021b). The Kröner model is based on Eshelby's theory (Eshelby, 1957) and considers a spherical particle embedded in an effective medium, satisfying both interface and compatibility conditions (Kroner, 1958). The model has been shown to accurately predict diffraction elastic constants that agree with experimental results (Wagner et al., 2014; Zhang et al., 2021b). The results in Table 2 indicate that the {*hkl*} elastic moduli E_{hkl} values of the direct-aged material agree well with the Kröner model predictions. In contrast, those of the as-built material deviate from the predictions by about 4.3%. For the {*hkl*} Poisson's ratio, the measured values of the direct-aged material are also closer to those of the predictions. These findings suggest that the anisotropic elasticity and plasticity behavior at the grain scale of the as-built material are affected by its non-equilibrium microstructure and residual strains.

3.6 Evolution of dislocations

The plastic activity can be detected by analyzing the FWHM values of diffraction peaks. When plastic activity occurs, the dislocation density changes, which in turn affects the FWHM value. As shown in Fig. 11(a), in zone rA (the elasticity stage), the FWHM values of the as-built material remain nearly constant, with variations smaller than 0.9%, indicating that no dislocation activity is present. In zone rB1 (the microplasticity stage 1), the FWHM values of the as-built material decrease apparently, with a reduction of -5.7% for the {311} peak, indicating the initiation of dislocation activity and a reduction in dislocation density. In zones rB2 and rC (the microplasticity stage 2 and the macroplasticity stage), the FWHM values of the as-built material increase continuously and obviously, revealing increased dislocation density. On the other hand, as shown in Fig. 11(b), the FWHM values of the direct-aged material are almost constant in zone rA (the elasticity stage), indicating the absence of dislocation activity. In zones rB, rC1, and rC2 (all microplasticity and macroplasticity stages), the FWHM values of the direct-aged material increase continuously and largely, indicating active dislocation multiplication.

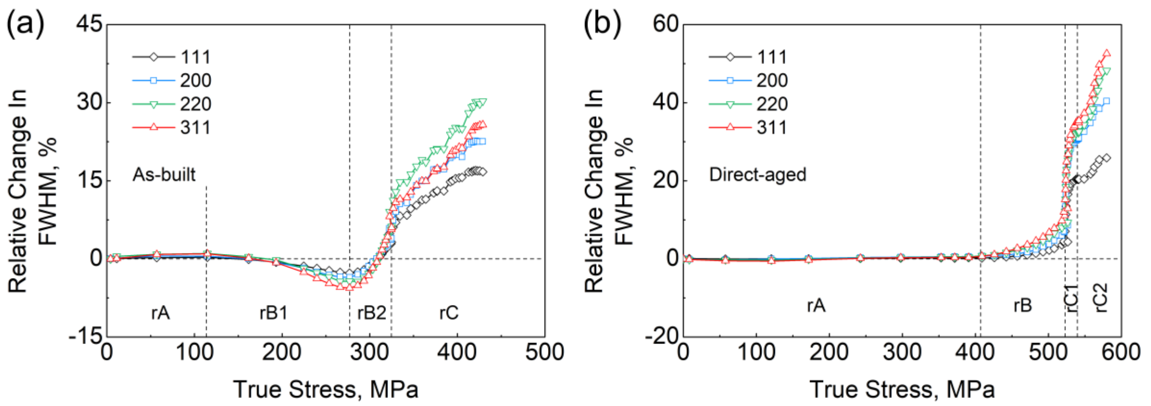

Fig. 11 Relative change in FWHM for the (a) as-built and (b) direct-aged specimens. The definitions of zones rA, rB, rB1, rB2, rC, rC1, and rC2 are the same as those in Fig. 10.

The variation of dislocation density can also be assessed using the mWH method (Ungar et al., 1999). The mWH function reads

$$\Delta K = 0.9/D + \left(\pi M_{\mathrm{K}}^{2} b^{2}/2\right)^{1/2} \rho^{1/2}\left(KC^{1/2}\right) + O\left(K^{2}C\right), \quad (5)$$

where $K = 2\sin\theta/\lambda$, with θ and λ being the diffraction angle and the X-ray wavelength, respectively; D is the average crystal size, M_{K} a material constant, b the magnitude of the Burgers vector, C the average contrast factor, and $O\left(K^{2}C\right)$ represents higher-order terms. Fig. 12 shows the mWH plot for the as-built and direct-aged specimens, which reveals qualitative features of peak broadening at different deformation stages. The mWH plot takes into account the strain anisotropy using the dislocation contrast factor C, so that the FWHM values (ΔK) vs. $KC^{1/2}$ values follow straight lines. In the mWH plot, the straight-line slope is proportional to the dislocation density. Fig. 12(a) shows that the line slope for the applied true stress of 272.1 MPa is lower than that for the applied stress of 8.0 MPa. This indicates that the dislocation density of the as-built specimen decreases during the microplasticity stage 1, which agrees with the FWHM results in Fig. 11(a). This dislocation density reduction may be associated with the relaxation of initial residual stresses, which are prone to develop in AM alloys (Zhang et al., 2022). At the applied stresses of 316.7 MPa and higher, the line slope increases again. Fig. 12(b) shows that the line slope only slightly increases when the applied stress increases to 450.3 MPa. At the applied stresses of 522.9 MPa and higher, the line slope rises significantly. These results from the mWH plot confirm the variation tendencies of dislocation density.

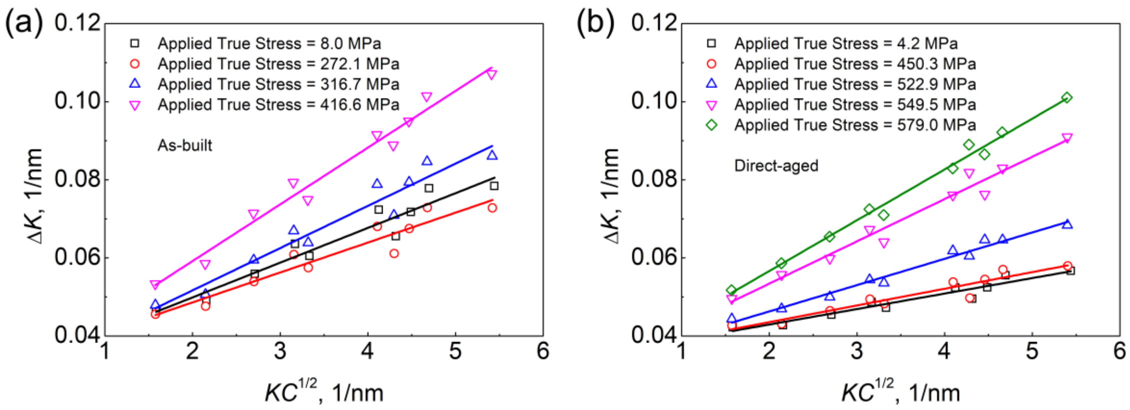

Fig. 12 Modified Williamson-Hall plot for the (a) as-built and (b) direct-aged specimens.

The CMWP analysis was employed to determine the quantitative evolution of dislocation density, as presented in Fig. 13(a). The initial dislocation density values of the as-built and direct-aged materials were found to be 8.13×10^{14} and 4.19×10^{14} m^{-2}, respectively. Therefore, the direct-aging treatment considerably reduced the initial dislocation density, which is consistent with the FWHM pole figure results in Fig. 7. The dislocation density of the as-built material reached 33.66×10^{14} m^{-2} in the as-built material at the true strain of 0.121, whereas that of the direct-aged material reached 47.69×10^{14} m^{-2} at the true strain of 0.081. During the macroplasticity stage, the dislocation density increased much faster in the direct-aged material than in the as-built material. This observation is mainly attributed to the higher density of Al_3(Sc, Zr) precipitates in the direct-aged material. The strong interactions between the dislocations and the coherent $Al_3(Sc, Zr)$ precipitates promote more pronounced dislocation multiplication during plastic deformation.

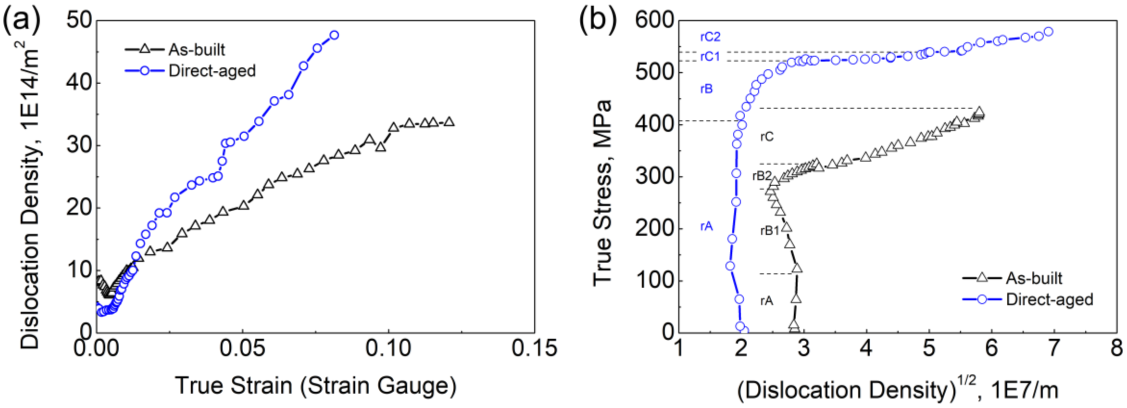

Fig. 13 Evolution of dislocation density: (a) dislocation density vs. true strain measured from strain gauge; (b) true stress vs. square root of dislocation density. In sub-figure (b), the definitions of zones rA, rB, rB1, rB2, rC, rC1, and rC2 are the same as those in Fig. 10.

Fig. 13(b) shows the true stress as a function of the square root of dislocation density, which also indicates the four zones defined in Fig. 10 for both materials. In the as-built material, the dislocation density in zone rA (elasticity stage) remains nearly constant, decreases evidently in zone rB1 (microplasticity stage 1), in agreement with the FWHM results in Fig. 11(a) and the mWH plot in Fig. 12(a). Subsequently, the dislocation density increases again in zone rB2 (microplasticity stage 2) and zone rC (macroplasticity stage) due to dislocation multiplication. Fig. 13(b) shows that the dislocation density remains almost constant in zone rA (elasticity) for the direct-aged material. In zone rB (microplasticity stage), the dislocation density increases continuously. No reduction in dislocation density is observed in the microplasticity stage of the direct-aged material. In zone rC1 and rC2 (macroplasticity stages 1 and 2), the dislocation density increases rapidly with a slight increase in true stress. These results are consistent with the FWHM results in Fig. 11(b) and the mWH plot in Fig. 12(b).

4. Crystal plasticity modeling based on dislocation density

Crystal plasticity models are widely used to study the deformation behavior of crystalline materials under various loading conditions. Crystal plasticity models can be broadly classified into two types: mean-field models and full-field models. The first type of crystal plasticity models includes the full constraint Taylor scheme (Mánik and Holmedal, 2014) and self-consistent schemes like the viscoplastic self-consistent (VPSC) model (Beyerlein and Tome, 2008; Zecevic et al., 2017) and elastoplastic self-consistent (EPSC) model (Daroju et al., 2022; Ghorbanpour et al., 2017). Mean-field models treat each single crystal grain as an ellipsoidal that embeds in and interacts only with the homogeneous effective medium. On the other hand, full-field models such as the crystal plasticity finite element (CPFE) model (Azhari et al., 2022; Chen et al., 2019; Li et al., 2020b; Zhang et al., 2022) and CPFFT model (Dadhich and Alankar, 2022; Sedighiani et al., 2020; Sedighiani et al., 2021) can directly use real grain microstructure as input, spatially resolve the grains, and calculate the mechanical fields in all grains. As a result, the grain-grain interactions and mechanical fields within grains and across grain boundaries can be investigated. In this study, CPFFT models are developed to investigate the deformation behavior of the as-built and direct-aged specimens.

4.1 Constitutive law

The CPFFT modeling in this study uses a constitutive model modified from the one published in the previous reports (Roters et al., 2019; Sedighiani et al., 2020; Wong et al., 2016), which relates the evolution of dislocation densities to dislocation multiplication, dislocation annihilation, and dipole formation. The difference between the present model and the previous one is that the interaction matrix used to calculate the athermal component of resolved shear stress is modified. In brief, the used CP constitutive model in this study can be described as follows.

The shear rate $\dot{\gamma}^{\alpha}$ of the slip system α is calculated by the Orowan equation:

$$\dot{\gamma}^{\alpha} = \rho_{\mathrm{m}}^{\alpha} b v^{\alpha}, \tag{6}$$

where $\rho_{\mathrm{m}}^{\alpha}$ is the mobile dislocation density, v^{α} the average velocity of mobile dislocations.

The average velocity v^{α} is determined by (Cereceda et al., 2016; Sedighiani et al., 2020)

$$v^{\alpha} = \frac{v_{\mathrm{b}}^{\alpha} v_{\mathrm{r}}^{\alpha}}{v_{\mathrm{b}}^{\alpha} + v_{\mathrm{r}}^{\alpha}}, \tag{7}$$

with

$$v_{\mathrm{r}}^{\alpha} = \frac{\tau_T^{*\alpha} b}{B}, \tag{8}$$

where B is the drag coefficient and $\tau_T^{*\alpha}$ the thermal stress defined by Eq. (10).

The velocity v_{b}^{α} is described by (Sedighiani et al., 2020)

$$v_{\mathrm{b}}^{\alpha} = v_0 \exp\left\{ -\frac{\Delta F}{k_{\mathrm{B}} T} \left[1 - \left(\frac{\tau_T^{*\alpha}}{\tau_0^{*}} \right)^{p} \right]^{q} \right\} \mathrm{sign}\left(\tau^{\alpha}\right), \tag{9}$$

where ΔF is the total short-range barrier energy, v_0 the dislocation glide velocity pre-factor, p and q determine the shape of the short-range barrier, τ_0^{*} the barrier's strength. The thermal stress $\tau_T^{*\alpha}$ is calculated by

$$\tau_T^{*\alpha} = \begin{cases} \left|\tau^{\alpha}\right| - \tau_{\mathrm{dis}}^{\alpha} & \text{for} \quad \left|\tau^{\alpha}\right| > \tau_{\mathrm{dis}}^{\alpha} \\ 0 & \text{for} \quad \left|\tau^{\alpha}\right| \le \tau_{\mathrm{dis}}^{\alpha} \end{cases}, \tag{10}$$

where τ^{α} is the total resolved shear stress on the slip system α.

The athermal component of the resolved shear stress $\tau_{\mathrm{dis}}^{\alpha}$ is defined as

$$\tau_{\mathrm{dis}}^{\alpha} = \mu b \left[\sum_{\beta=1}^{N_{\mathrm{s}}} f_{\mathrm{e}} \xi_{\alpha\beta} \left(\rho_{\mathrm{m}}^{\beta} + \rho_{\mathrm{d}}^{\beta} \right) \right]^{1/2}, \tag{11}$$

where μ is the shear modulus, N_{s} the number of slip system, f_{e} a positive coefficient, $\xi_{\alpha\beta}$ the interaction matrix between slip systems α and β, $\rho_{\mathrm{d}}^{\beta}$ the dislocation dipole density of the slip system β. The introduction of the f_e parameter is based on previous observations. The interaction matrix $\xi_{\alpha\beta}$ is first introduced by (Franciosi et al., 1980) to allow slip-system-dependent interaction coefficients. $\xi_{\alpha\beta}$ is a generalized version of the dislocation strengthening coefficient α_dis in the well-known Taylor model. The experimental values of α_dis exhibit a large scatter (Bahl et al., 2017), e.g., 0.15< α_dis <0.9 has been measured for copper (Lavrentev, 1980). More details about the scatter values of α_dis have been summarized and discussed in the two review articles (Mughrabi, 2016; Sauzay and Kubin, 2011). Based on previous observations, the f_e parameter is introduced in the present modeling, which allows scaling the interaction matrix $\xi_{\alpha\beta}$, making the present model different from the previous one where f_e is fixed to 1 (Madivala et al., 2018; Sedighiani et al., 2020; Wong et al., 2016). For the FCC metals, the dimensionless components of the interaction matrix $\xi_{\alpha\beta}$ determined via dislocation dynamics simulations are 0.122 for self-interaction, 0.122 for coplanar interaction, 0.625 for collinear interaction, 0.07 for Hirth lock, 0.137 for glissile junction, and 0.122 for Lomer lock (Kubin et al., 2008).

The mobile dislocation density evolution rate is given by

$$\dot{\rho}_\mathrm{m}^\alpha = \frac{1}{\Lambda^\alpha}\frac{\left|\dot{\gamma}^\alpha\right|}{b} - 2d_\mathrm{dipole}^\alpha \rho_\mathrm{m}^\alpha \frac{\left|\dot{\gamma}^\alpha\right|}{b}, \tag{12}$$

The first term on the right side of Eq. (12) denotes the dislocation multiplication rate, which is determined by the dislocation mean free path Λ^α with

$$\frac{1}{\Lambda^\alpha} = \frac{1}{d_\mathrm{c}} + \frac{1}{\lambda^\alpha}. \tag{13}$$

Here, d_c is the average cell size. Besides,

$$\frac{1}{\lambda^\alpha} = \frac{1}{C_\lambda}\left[\sum_{\beta=1}^{N_\mathrm{s}} g_{\alpha\beta}\left(\rho_\mathrm{m}^\beta + \rho_\mathrm{d}^\beta\right)\right]^{1/2}, \tag{14}$$

where C_λ is a material parameter controlling the number of dislocations that a mobile dislocation passes before it is trapped by forest dislocations (Ma and Roters, 2004), $g_{\alpha\beta}$ is the projection matrix for the forest dislocation density (Roters et al., 2019).

The second term on the right side of Eq. (12) represents the immobilization of the mobile dislocation density due to dipole formation. The critical distance for dipole formation is calculated by (Roters et al., 2019; Wong et al., 2016)

$$d_{\mathrm{dipole}}^{\alpha}=\frac{3\mu b}{16\pi\left|\tau^{\alpha}\right|}\,. \tag{15}$$

The evolution rate of the immobile dislocation dipole density follows (Roters et al., 2019; Sedighiani et al., 2020)

$$\dot{\rho}_{\mathrm{d}}^{\alpha}=2\left(d_{\mathrm{dipole}}^{\alpha}-d_{\mathrm{anni}}^{\alpha}\right)\rho_{\mathrm{m}}^{\alpha}\frac{\left|\dot{\gamma}^{\alpha}\right|}{b}-2d_{\mathrm{anni}}^{\alpha}\rho_{\mathrm{d}}^{\alpha}\frac{\left|\dot{\gamma}^{\alpha}\right|}{b}, \tag{16}$$

where the critical distance $d_{\mathrm{anni}}^{\alpha}$ for two mobile dislocations with opposite signs to annihilate is given by

$$d_{\mathrm{anni}}^{\alpha}=C_{\mathrm{anni}}b\,. \tag{17}$$

The first term on the right side of Eq. (16) reflects that a dislocation dipole forms when two mobile dislocations have a distance larger than $d_{\mathrm{anni}}^{\alpha}$ but smaller than the critical distance for dipole formation $d_{\mathrm{dipole}}^{\alpha}$ (Sedighiani et al., 2020). The second term on the right side of Eq. (16) corresponds to the annihilation of dislocation dipoles.

The total dislocation density $\rho_{\mathrm{total}}^{\alpha}$ of slip system α is the summation of the mobile dislocation density and the immobile dislocation dipole density, which is

$$\rho^{\alpha}=\rho_{\mathrm{m}}^{\alpha}+\rho_{\mathrm{d}}^{\alpha}\,. \tag{18}$$

4.2 Microstructure models and simulation approach

Periodic three-dimensional (3D) microstructure models with physical dimensions of 7.04×7.04×7.04 μm^3 were generated for both as-built and direct-aged specimens. All microstructure models were discretized into 128×128×128 (=2,097,152) voxels. The volume fraction of porosity was set to 0.44%

based on measurement. The $Al_3(Sc, Zr)$ particle volume fraction was set to 1.82% for the direct-aged specimen (Patil, 2020). The Al grain orientations were generated using the measured textures (Fig. 6). The crystallographic orientations of the $Al_3(Sc, Zr)$ particles were assumed to be random. The generated 3D virtual microstructure models are shown in Fig. 14 for the as-built and direct-aged specimens. The microstructure model for the as-built specimen includes 1356 Al grains and 78 pores (Fig. 14(a)); the microstructure model for the direct-aged specimen contains 1354 Al grains, 76 pores, and 4767 $Al_3(Sc, Zr)$ particles (Fig. 14(b)).

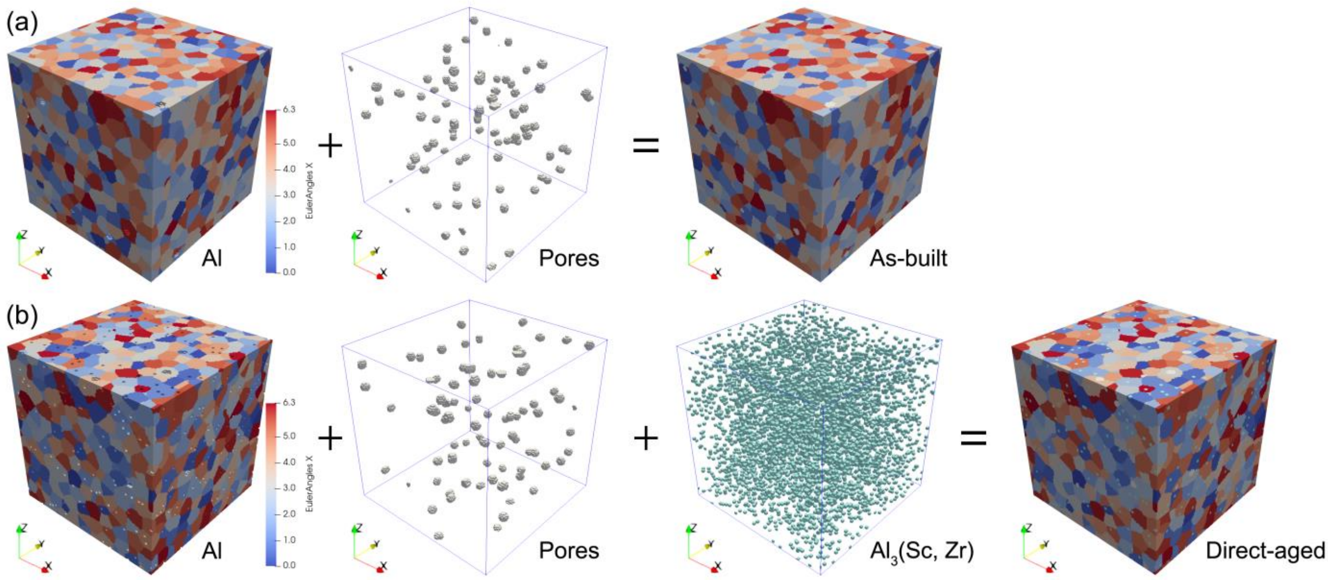

Fig. 14 Virtual microstructures used in the CPFFT simulations for (a) the as-built specimen and (b) the direct-aged specimen.

The CPFFT models were solved using the fast-Fourier-transform-based spectral solver implemented in the DAMASK software (Roters et al., 2019). Periodic boundary conditions were employed, and the tensile loading direction was set along the Z-axis direction of the microstructure models. The fitted and cited material parameters used in the CPFFT simulations are listed in Table 3. A parameter sensitivity analysis for the CPFFT model is shown in Section S1 of Supplementary Materials. Although local deformation causes fluctuations in strain rates, as shown in Fig. 4, the instantaneous strain rates are smaller than 3.0×10^{-3} s^{-1} and are within the quasi-static condition. Therefore, the effect of fluctuating strain rates on the mechanical properties is expected to be small. To simplify the modeling process, we assume that the deformation is under a uniform rate, and the tensile strain rate of the CPFFT simulations was set to 3.0×10^{-4} s^{-1}, the same as the nominal strain rate of the in-situ experiments.

Table 3 Fitted and cited material parameters used for the CPFFT simulations.

Phase	Parameter	Value		Reference
Al	C_{11}	108.2 GPa		(Zhang et al., 2021c)
	C_{12}	61.3 GPa		
	C_{44}	28.5 GPa		
	v_0	1.0×10^{-2} m/s	for As-built	
		1.0×10^{-5} m/s	for Direct-aged	
	ΔF	3.5×10^{-19} J	for As-built	
		4.0×10^{-19} J	for Direct-aged	
	p	0.70	for As-built	
		0.66	for Direct-aged	
	q	1.60	for As-built	
		1.54	for Direct-aged	
	τ_0^*	125 MPa	for As-built	
		266 MPa	for Direct-aged	
	B	5.0×10^{-4} Pa·s		
	f_e	0.35	for As-built	
		0.05	for Direct-aged	
	C_λ	15.0	for As-built	
		4.0	for Direct-aged	
	C_{anni}	1.0	for As-built	
		0.6	for Direct-aged	
$Al_3(Sc, Zr)$	C_{11}	184.41 GPa		(Hu et al., 2013)
	C_{12}	40.02 GPa		
	C_{44}	74.65 GPa		

4.3 Simulation results

Fig. 15 compares the predicted properties from the CPFFT simulations with the measured properties from the in-situ SXRD experiment for both as-built and direct-aged specimens. The CPFFT models reproduce the macroscopic stress-strain curves very well for both specimens (Figs. 15(a)-(b)). In the elastic stage of the as-built specimen, the predicted Al {311} lattice strain curves coincide with measurements, and basically capture the nonlinearity in the microplasticity and macroplasticity stages (Fig. 15(c)). For the direct-aged specimen, the predicted {311} lattice strain curves agree well with the experimental results (Fig. 15(d)). Comparison between predicted and measured {111}, {200}, and {220} lattice strains are shown in Supplementary Fig. S15, which confirms reasonable prediction accuracy. The predicted evolutions of the total dislocation densities agree with in-situ measured results in general, despite some local deviations (Figs. 15(e)-(f)). For example, the model does not predict the small reduction in total dislocation density during the microplasticity stage 1 of the as-built specimen (Fig. 15(e)). This inconsistency is likely related to the fact that the current CPFFT neglect the initial residual stresses in the as-built specimen. Besides, the predicted total dislocation density values of the direct-aged specimen are lower than the measured values when the true strains are between 0.006 and 0.066, beyond which the situation reverses (Fig. 15(f)). In fact, the second-order variation tendency of the measured dislocation density curve in Fig. 15(f) is similar to that of the measured instantaneous strain rate curve in Fig. 4(d). Accordingly, the discrepancy between the predicted and measured dislocation density of the direct-aged specimen is likely associated with the effects of fluctuating strain rates, while the current CPFFT model assumes a uniform strain rate. Despite these local deviations, the predicted macro- and microscopic properties from the CPFFT simulations agree with the in-situ experimental results.

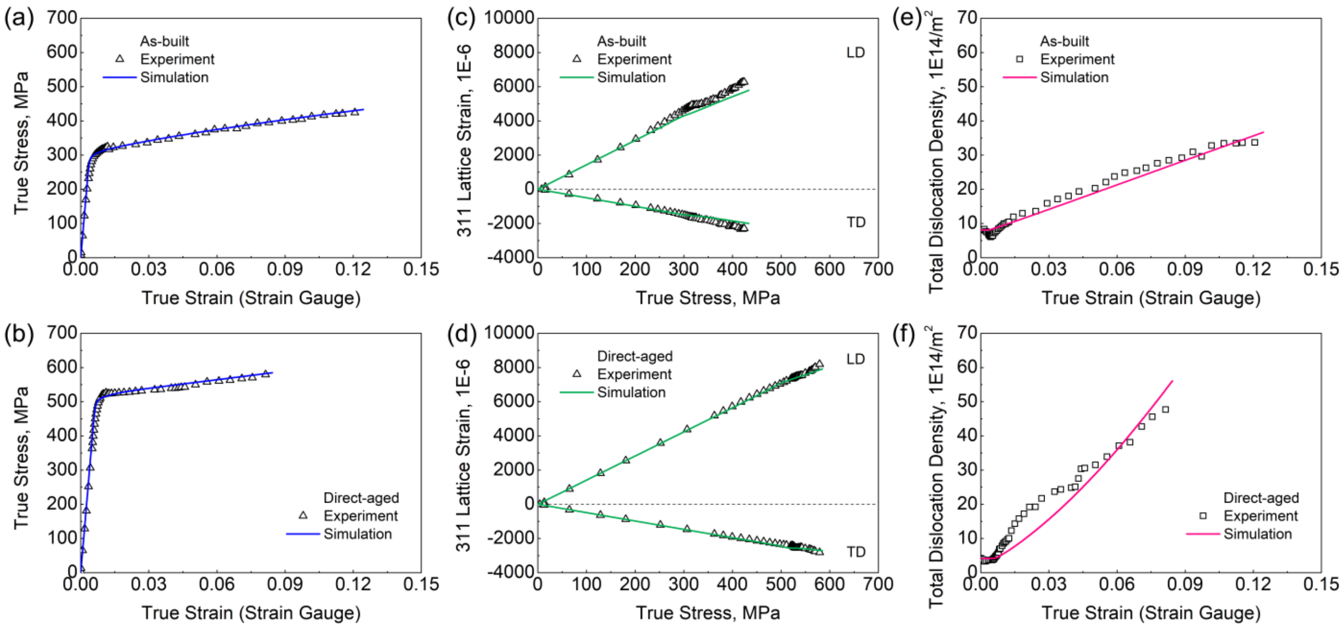

Fig. 15 Comparison between predicted and measured results: (a)-(b) macroscopic true stress-strain curves, (c)-(d) {311} lattice strains, and (e)-(f) total dislocation density for the as-built specimen.

Fig. 16 illustrates the micromechanical fields predicted for the as-built specimen under two different applied true stresses: 290 MPa (microplasticity stage 2) and 404 MPa (macroplasticity stage). In Fig. 16(a), the gray grains remain in elastic deformation, while many blue and green grains have entered the microplasticity stage with an increased total dislocation density. Although the effective plastic strain map (Fig. 16(b)) appears in different color shades from the total dislocation density map (Fig. 16(a)), the two are similar because dislocations are the basic carriers of plastic deformation.

Upon comparing Figs. 16(a) and (c), it can be observed that the grains with high Mises stress values (yellow and red regions in Fig. 16(c)) essentially correspond to the grains undergoing elastic deformation (gray regions in Fig. 16(a)). In contrast, grains with medium Mises stress values (green regions in Fig. 16(c)) represent the grains entering the microplasticity stage (blue and green regions in Fig. 16(a)). These results confirm that load transfer occurs from soft grains to hard grains during microplasticity deformation.

Furthermore, Fig. 16(c) demonstrates that the presence of pores induces stress concentrations, triggering multiple slip systems (X-shaped blue regions in Fig. 16(a)) around the pores. These stress concentrations also result in higher total dislocation densities in regions surrounding the pores compared to regions further away. These findings reveal that pores significantly affect microplasticity behavior and reduce the proportional limit. As the applied true stress reaches 404 MPa in the macroplasticity stage, the dislocation densities in most regions exhibit significant increases (Fig. 16(d)). Thick and large X-shaped green regions with high dislocation densities are frequently observed in Fig. 16(d), indicating multiple slip and slip transitions across grain boundaries. The gray regions in Fig. 16(d) indicate that the dislocation densities either remain at the same level before deformation or exhibit a minimal increase. The effective plastic strain map in Fig. 16(e) demonstrates a similar feature to the total dislocation density map in Fig. 16(d). Regarding the stress field, the hot grains with high von Mises stress values in the macroplasticity stage (Fig. 16(f)) are mainly the same hot grains with yellow and red colors in the microplasticity stage (Fig. 16(c)). These hot grains are harder than other green and blue grains, resulting in higher stress levels due to the load transfer effect.

Fig. 17(a) displays that the high dislocation density regions in the microplasticity stage (applied stress is 509 MPa) of the direct-aged specimen are composed of thin, parallel slip traces. This is different from the slip image in the microplasticity stage of the as-built specimen illustrated in Fig. 16(a), where the high dislocation regions are represented by blue islands. This difference should be related to the presence of Al_3(Sc, Zr) particles, which impede the movements of mobile dislocations. Consequently, mobile dislocations have to find their slip path between the Al_3(Sc, Zr) particles (small cubic particles), forming the narrow slip traces in Fig. 17(a). Supplementary section S3 confirms this, where Fig. S16 indicates that without Al_3(Sc, Zr) particles, the plastic deformation pattern changes and becomes similar to that of the as-built specimen. The Al matrix connected to the top and bottom sides of the $Al_3(Sc, Zr)$ particles exhibits increased dislocation densities. Similar to the as-built specimen, high dislocation density regions with green and yellow colors are observed surrounding the round pores.

Fig. 17(b) confirms that round pores cause strain concentrations around them. Fig. 17(c) reveals that small cubic $Al_3(Sc, Zr)$ particles (red color) bear high stresses, reflecting a load transfer strengthening effect. Surprisingly, Fig. 17(c) indicates that the round pores in the direct-aged specimen do not cause obvious stress concentrations in the surrounding Al matrix, which is different from the case in the as-built specimen. Additionally, hard Al grains (yellow and red color) also experience high stresses due to the load transfer effect between grains.

In the macroplasticity stage of the direct-aged specimen, where the applied stress increased to 569 MPa, a much more heterogeneous deformation pattern is observed in the total dislocation density distribution, characterized by scattered, small, and narrow hot regions (Fig. 17(d)). This differs from the as-built specimen, where the hot regions are broader and more continuous (Fig. 16(d)). Besides, the hot regions in the direct-aged specimen exhibit significantly higher dislocation densities, with a maximum total dislocation density of 5.37×10^{16} m^{-2} as shown in Fig. 17(d), compared to a maximum of 1.26×10^{16} m^{-2} in the as-built specimen (Fig. 16(d)). Moreover, intergranular and interphase heterogeneous distribution of stress is apparent in the direct-aged specimen (Fig. 17(f)). These results support the conclusion that the direct-aged material has a lower elongation than the as-built material.

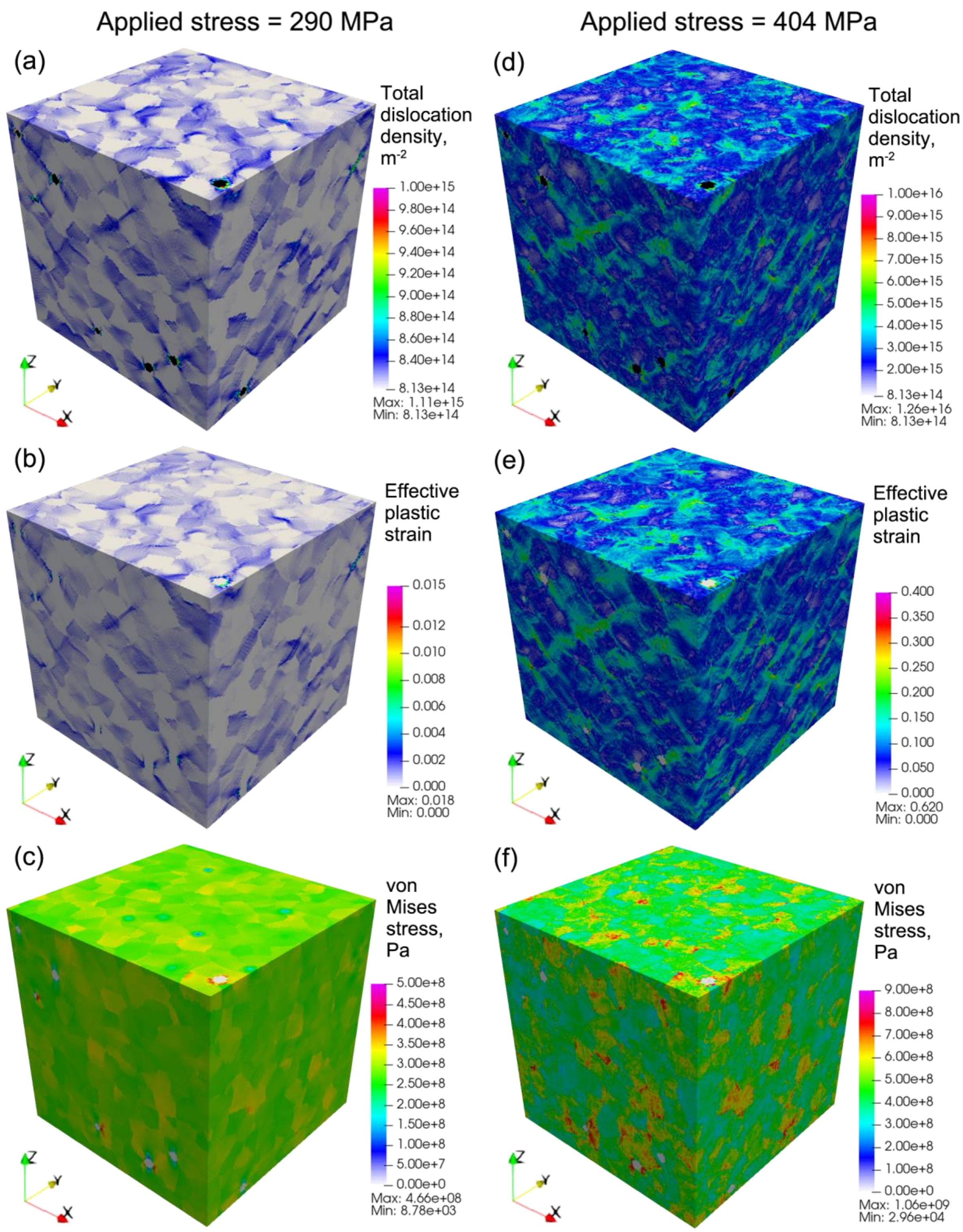

Fig. 16 Predicted micromechanical fields of the as-built specimen: (a) total dislocation density, (b) effective plastic strain, and (c) von Mises stress fields at the applied true stress of 290 MPa (microplasticity stage 2); (d) total dislocation density, (e) effective plastic strain, and (f) von Mises stress fields at the applied true stress of 404 MPa (macroplasticity stage).

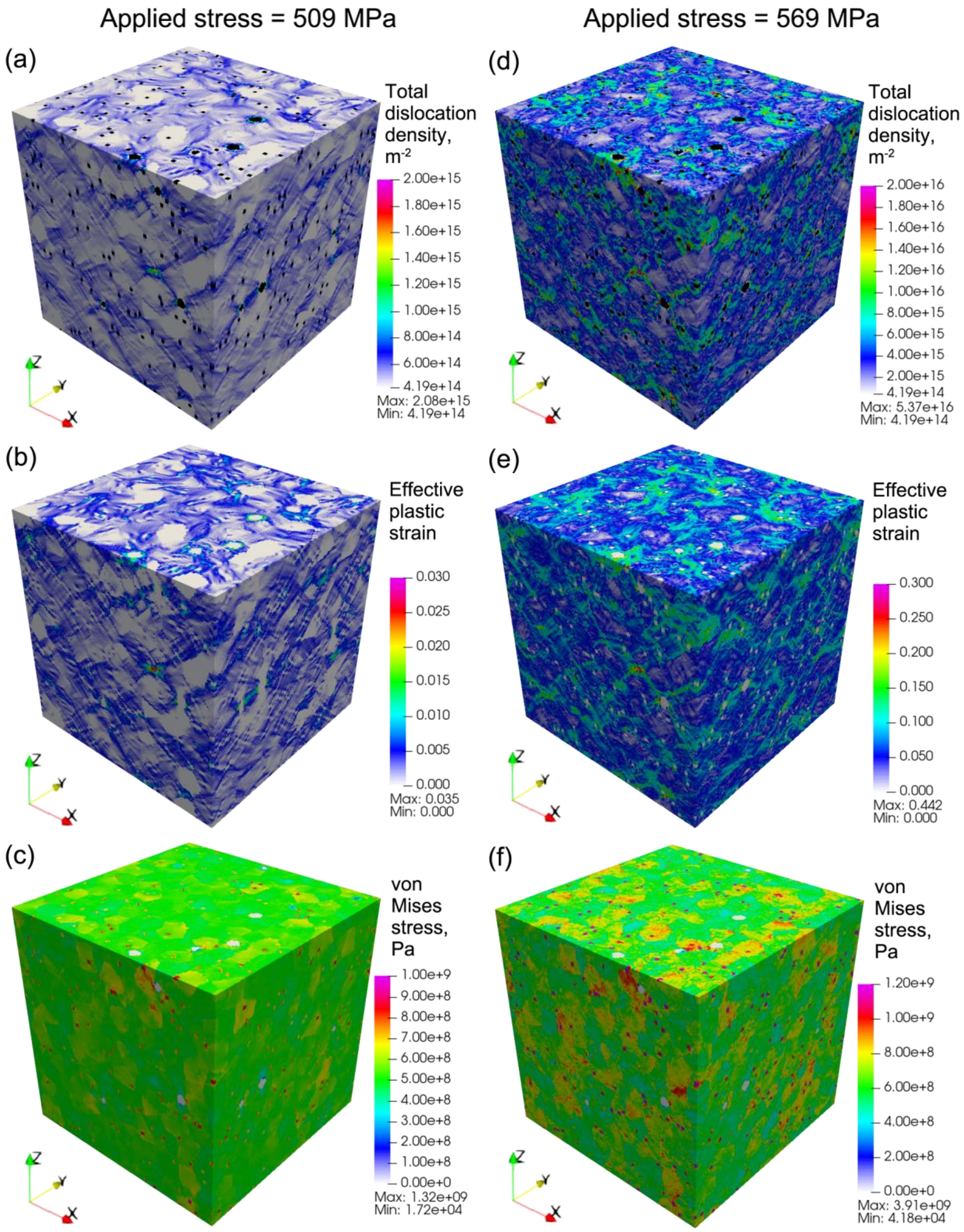

Fig. 17 Predicted micromechanical fields of the direct-aged specimen: (a) total dislocation density, (b) effective plastic strain, and (c) von Mises stress fields at the applied true stress of 509 MPa (microplasticity stage); (d) total dislocation density, (e) effective plastic strain, and (f) von Mises stress fields at the applied true stress of 569 MPa (macroplasticity stage).

5. Conclusions

(1) The micromechanical behavior of the as-built specimen (additively manufactured Al-Mg-Sc-Zr alloy) under continuous tensile loading can be divided into four stages: the elasticity stage, followed by the microplasticity stages 1 and 2, and finally, the macroplasticity stage. In contrast, the direct-aged specimen also shows four but different stages: the elasticity stage, followed by the microplasticity stage, and finally, the macroplasticity stages 1 and 2.

(2) The dislocation density decreases during the microplasticity stage 1 of the as-built specimen, but increases in the subsequent plastic deformation stages. After direct aging, the dislocation density decreases due to the annealing effect. However, no reduction in the dislocation density is observed during the microplasticity stage of the direct-aged specimen. The dislocation density increases continuously during the micro- and macroplasticity stages.

(3) The present CPFFT model effectively predicts the macro- and microscopic mechanical behavior of both as-built and direct-aged specimens. The predicted stress-strain curves, lattice strains, and dislocation density agree well with the in-situ measured values. However, the CPFFT model does not perfectly capture the local fluctuations in dislocation density during plastic deformation due to the exclusion of some physical mechanisms.

(4) The CPFFT simulations demonstrate heterogeneous stress and strain distribution during micro- and macroplastic deformation in both specimens. The presence of pores causes stress or strain concentrations, triggering multiple slip systems around them and resulting in higher dislocation densities in nearby regions. The plastic deformation and corresponding dislocation distribution are more heterogeneous in the direct-aged specimen due to the presence of $Al_3(Sc, Zr)$ particles, resulting in a shorter elongation of the direct-aged specimen compared to the as-built one.

Acknowledgments

The authors are very grateful to the GEMS-P staff at DESY, Hamburg, Germany, for their kind support of the experiments with proposal No. H-20010018. We also acknowledge our gratitude and appreciation to our partners, Daimler AG, Premium AEROTEC GmbH, and EOS GmbH within the NextGenAM project for their contribution during the development of various ideas, concepts, and test specimens.

References

Aboulkhair, N.T., Everitt, N.M., Ashcroft, I., Tuck, C., 2014. Reducing porosity in AlSi10Mg parts processed by selective laser melting. Addit. Manuf. 1-4, 77-86.

Arechabaleta, Z., van Liempt, P., Sietsma, J., 2016. Quantification of dislocation structures from anelastic deformation behaviour. Acta Mater. 115, 314-323.

Azhari, F., Wallbrink, C., Sterjovski, Z., Crawford, B.R., Menzel, A., Agius, D., Wang, C.H., Schaffer, G., 2022. Predicting the complete tensile properties of additively manufactured Ti-6Al-4V by integrating three-dimensional microstructure statistics with a crystal plasticity model. Int. J. Plast. 148, 103127.

Bahl, S., Suwas, S., Ungar, T., Chatterjee, K., 2017. Elucidating microstructural evolution and strengthening mechanisms in nanocrystalline surface induced by surface mechanical attrition treatment of stainless steel. Acta Mater. 122, 138-151.

Bayoumy, D., Kwak, K., Boll, T., Dietrich, S., Schliephake, D., Huang, J., Yi, J., Takashima, K., Wu, X., Zhu, Y., Huang, A., 2022. Origin of non-uniform plasticity in a high-strength Al-Mn-Sc based alloy produced by laser powder bed fusion. J. Mater. Sci. Technol. 103, 121-133.

Benallal, A., Berstad, T., Borvik, T., Hopperstad, O.S., Koutiri, I., de Codes, R.N., 2008. An experimental and numerical investigation of the behaviour of AA5083 aluminium alloy in presence of the Portevin-Le

Chatelier effect. Int. J. Plast. 24, 1916-1945.

Berger, A., Witz, J.F., El Bartali, A., Sadat, T., Limodin, N., Dubar, M., Najjar, D., 2022. Experimental investigation of early strain heterogeneities and localizations in polycrystalline α-Fe during monotonic loading. Int. J. Plast. 153, 103253.

Beyerlein, I.J., Tome, C.N., 2008. A dislocation-based constitutive law for pure Zr including temperature effects. Int. J. Plast. 24, 867-895.

Cereceda, D., Diehl, M., Roters, F., Raabe, D., Perlado, J.M., Marian, J., 2016. Unraveling the temperature dependence of the yield strength in single-crystal tungsten using atomistically-informed crystal plasticity calculations. Int. J. Plast. 78, 242-265.

Chen, H., Chen, Z., Ji, G., Zhong, S.Y., Wang, H.W., Borbely, A., Ke, Y.B., Brechet, Y., 2021a. Experimental and modelling assessment of ductility in a precipitation hardening AlMgScZr alloy. Int. J. Plast. 139, 102971.

Chen, H., Chen, Z., Ji, G., Zhong, S.Y., Wang, H.W., Borbely, A., Ke, Y.B., Brechet, Y., 2021b. The influence of shearable and nonshearable precipitates on the Portevin-Le Chatelier behavior in precipitation hardening AlMgScZr alloys. Int. J. Plast. 147, 103120.

Chen, W., Voisin, T., Zhang, Y., Forien, J.B., Spadaccini, C.M., McDowell, D.L., Zhu, T., Wang, Y.M., 2019. Microscale residual stresses in additively manufactured stainless steel. Nat. Commun. 10, 4338.

Choo, H., Koehler, M.R., White, L.P., Ren, Y., Morin, D., Garlea, E., 2020. Influence of defect characteristics on tensile deformation of an additively manufactured stainless steel: Evolutions of texture and intergranular strain. Mater. Sci. Eng. A 791, 139637.

Clausen, B., Lorentzen, T., Leffers, T., 1998. Self-consistent modelling of the plastic deformation of FCC polycrystals and its implications for diffraction measurements of internal stresses. Acta Mater. 46, 3087-

3098.

Cordova, L., Bor, T., de Smit, M., Carmignato, S., Campos, M., Tinga, T., 2020. Effects of powder reuse on the microstructure and mechanical behaviour of Al-Mg-Sc-Zr alloy processed by laser powder bed fusion (LPBF). Addit. Manuf. 36, 101625.

Curtin, W.A., Olmsted, D.L., Hector, L.G., Jr., 2006. A predictive mechanism for dynamic strain ageing in aluminium-magnesium alloys. Nat. Mater. 5, 875-880.

Dadhich, R., Alankar, A., 2022. A modular spectral solver for crystal plasticity. Int. J. Plast. 156, 103328.

Daroju, S., Kuwabara, T., Sharma, R., Fullwood, D.T., Miles, M.P., Knezevic, M., 2022. Experimental characterization and crystal plasticity modeling for predicting load reversals in AA6016-T4 and AA7021-T79. Int. J. Plast. 153, 103292.

Eshelby, J.D., 1957. The Determination of the Elastic Field of an Ellipsoidal Inclusion, and Related Problems. Proc. R. Soc. Lon. Ser.-A 241, 376-396.

Franciosi, P., Berveiller, M., Zaoui, A., 1980. Latent hardening in copper and aluminium single crystals. Acta Metallurgica 28, 273-283.

Ghorbanpour, S., Zecevic, M., Kumar, A., Jahedi, M., Bicknell, J., Jorgensen, L., Beyerlein, I.J., Knezevic, M., 2017. A crystal plasticity model incorporating the effects of precipitates in superalloys: Application to tensile, compressive, and cyclic deformation of Inconel 718. Int. J. Plast. 99, 162-185.

Herzog, D., Seyda, V., Wycisk, E., Emmelmann, C., 2016. Additive manufacturing of metals. Acta Mater. 117, 371-392.

Hu, W.C., Liu, Y., Li, D.J., Zeng, X.Q., Xu, C.S., 2013. Mechanical and thermodynamic properties of Al3Sc and Al3Li precipitates in Al-Li-Sc alloys from first-principles calculations. Phys. B 427, 85-90.

Jia, Q.B., Rometsch, P., Cao, S., Zhang, K., Wu, X.H., 2019a. Towards a high strength aluminium alloy development methodology for selective laser melting. Mater. Des. 174, 107775.

Jia, Q.B., Rometsch, P., Kurnsteiner, P., Chao, Q., Huang, A.J., Weyland, M., Bourgeois, L., Wu, X.H., 2019b. Selective laser melting of a high strength Al-Mn-Sc alloy: Alloy design and strengthening mechanisms. Acta Mater. 171, 108-118.

Khomutov, M., Chereshneva, A., Petrovskiy, P., Daubarayte, D., Cheverikin, V., Sova, A., Travyanov, A., Smurov, I., 2021. Microstructure of Al–Mg-Sc-Zr alloy cold spray deposits after heat treatment and hot isostatic pressing. J. Alloys Compd. 858, 157644.

Kroner, E., 1958. Berechnung der elastischen Konstanten des Vielkristalls aus den Konstanten des Einkristalls. Zeitschrift Fur Physik 151, 504-518.

Kubin, L., Devincre, B., Hoc, T., 2008. Modeling dislocation storage rates and mean free paths in face-centered cubic crystals. Acta Mater. 56, 6040-6049.

Lavrentev, F.F., 1980. The type of dislocation interaction as the factor determining work hardening. Mater. Sci. Eng. 46, 191-208.

Li, D.Y., Wagoner, R.H., 2021. The nature of yielding and anelasticity in metals. Acta Mater. 206, 116625.

Li, G., Zhao, N.Q., Liu, T., Li, J.J., He, C.N., Shi, C.S., Liu, E.Z., Sha, J.W., 2014. Effect of Sc/Zr ratio on the microstructure and mechanical properties of new type of Al-Zn-Mg-Sc-Zr alloys. Mater. Sci. Eng. A 617, 219-227.

Li, R.D., Wang, M.B., Li, Z.M., Cao, P., Yuan, T.C., Zhu, H.B., 2020a. Developing a high-strength Al-Mg-Si-Sc-Zr alloy for selective laser melting: Crack-inhibiting and multiple strengthening mechanisms. Acta Mater. 193, 83-98.

Li, R.D., Wang, M.B., Yuan, T.C., Song, B., Chen, C., Zhou, K.C., Cao, P., 2017. Selective laser melting of a novel Sc and Zr modified Al-6.2 Mg alloy: Processing, microstructure, and properties. Powder

Technol. 319, 117-128.

Li, Y.L., Kohar, C.P., Mishra, R.K., Inal, K., 2020b. A new crystal plasticity constitutive model for simulating precipitation-hardenable aluminum alloys. Int. J. Plast. 132, 102759.

Ma, A., Roters, F., 2004. A constitutive model for fcc single crystals based on dislocation densities and its application to uniaxial compression of aluminium single crystals. Acta Mater. 52, 3603-3612.

Maaß, R., Derlet, P.M., 2018. Micro-plasticity and recent insights from intermittent and small-scale plasticity. Acta Mater. 143, 338-363.

Madivala, M., Schwedt, A., Wong, S.L., Roters, F., Prahl, U., Bleck, W., 2018. Temperature dependent strain hardening and fracture behavior of TWIP steel. Int. J. Plast. 104, 80-103.

Mánik, T., Holmedal, B., 2014. Review of the Taylor ambiguity and the relationship between rate-independent and rate-dependent full-constraints Taylor models. Int. J. Plast. 55, 152-181.

Mughrabi, H., 2016. The α-factor in the Taylor flow-stress law in monotonic, cyclic and quasi-stationary deformations: Dependence on slip mode, dislocation arrangement and density. Curr. Opin. Solid State Mat. Sci. 20, 411-420.

Patil, Y., 2020. Influencing factors and material model for simulation-based prediction of mechanical properties of additively manufactured AlMgSc parts, Final project report.

Ribarik, G., Joni, B., Ungar, T., 2019. Global optimum of microstructure parameters in the CMWP line-profile-analysis method by combining Marquardt-Levenberg and Monte-Carlo procedures. J. Mater. Sci. Technol. 35, 1508-1514.

Ribarik, G., Ungar, T., 2010. Characterization of the microstructure in random and textured polycrystals and single crystals by diffraction line profile analysis. Mater. Sci. Eng. A 528, 112-121.

Rodriguez, P., 1984. Serrated plastic flow. Bull. Mater. Sci. 6, 653-663.

Roters, F., Diehl, M., Shanthraj, P., Eisenlohr, P., Reuber, C., Wong, S.L., Maiti, T., Ebrahimi, A., Hochrainer, T., Fabritius, H.O., Nikolov, S., Friak, M., Fujita, N., Grilli, N., Janssens, K.G.F., Jia, N., Kok, P.J.J., Ma, D., Meier, F., Werner, E., Stricker, M., Weygand, D., Raabe, D., 2019. DAMASK - The Dusseldorf Advanced Material Simulation Kit for modeling multi-physics crystal plasticity, thermal, and damage phenomena from the single crystal up to the component scale. Comp. Mater. Sci. 158, 420-478.

Sauzay, M., Kubin, L.P., 2011. Scaling laws for dislocation microstructures in monotonic and cyclic deformation of fcc metals. Prog. Mater Sci. 56, 725-784.

Scardi, P., Leoni, M., 2006. Line profile analysis: pattern modelling versus profile fitting. J. Appl. Crystallogr. 39, 24-31.

Scardi, P., Leoni, M., Delhez, R., 2004. Line broadening analysis using integral breadth methods: a critical review. J. Appl. Crystallogr. 37, 381-390.

Schimbäck, D., Mair, P., Bärtl, M., Palm, F., Leichtfried, G., Mayer, S., Uggowitzer, P.J., Pogatscher, S., 2022. Alloy design strategy for microstructural-tailored scandium-modified aluminium alloys for additive manufacturing. Scr. Mater. 207, 114277.

Schmidtke, K., 2020. Qualification of SLM: additive manufacturing for aluminium. PhD thesis. Hamburg University of Technology.

Schmidtke, K., Palm, F., Hawkins, A., Emmelmann, C., 2011. Process and Mechanical Properties: Applicability of a Scandium modified Al-alloy for Laser Additive Manufacturing. Phys. Procedia 12, 369-374.

Schroeder, J., Evans, A., Mishurova, T., Ulbricht, A., Sprengel, M., Serrano-Munoz, I., Fritsch, T., Kromm, A., Kannengiesser, T., Bruno, G., 2021. Diffraction-Based Residual Stress Characterization in Laser Additive Manufacturing of Metals. Metals 11, 1830.

Sedighiani, K., Diehl, M., Traka, K., Roters, F., Sietsma, J., Raabe, D., 2020. An efficient and robust approach to determine material parameters of crystal plasticity constitutive laws from macro-scale stress-strain curves. Int. J. Plast. 134, 102779.

Sedighiani, K., Shah, V., Traka, K., Diehl, M., Roters, F., Sietsma, J., Raabe, D., 2021. Large-deformation crystal plasticity simulation of microstructure and microtexture evolution through adaptive remeshing. Int. J. Plast. 146, 103078.

Shi, Y.J., Rometsch, P., Yang, K., Palm, F., Wu, X.H., 2017. Characterisation of a novel Sc and Zr modified Al-Mg alloy fabricated by selective laser melting. Mater. Lett. 196, 347-350.

Shi, Y.J., Yang, K., Kairy, S.K., Palm, F., Wu, X.H., Rometsch, P.A., 2018. Effect of platform temperature on the porosity, microstructure and mechanical properties of an Al-Mg-Sc-Zr alloy fabricated by selective laser melting. Mater. Sci. Eng. A 732, 41-52.

Spierings, A.B., Dawson, K., Dumitraschkewitz, P., Pogatscher, S., Wegener, K., 2018a. Microstructure characterization of SLM-processed Al-Mg-Sc-Zr alloy in the heat treated and HIPed condition. Addit. Manuf. 20, 173-181.

Spierings, A.B., Dawson, K., Heeling, T., Uggowitzer, P.J., Schaublin, R., Palm, F., Wegener, K., 2017. Microstructural features of Sc- and Zr-modified Al-Mg alloys processed by selective laser melting. Mater. Des. 115, 52-63.

Spierings, A.B., Dawson, K., Uggowitzer, P.J., Wegener, K., 2018b. Influence of SLM scan-speed on microstructure, precipitation of Al3Sc particles and mechanical properties in Sc- and Zr-modified Al-Mg alloys. Mater. Des. 140, 134-143.

Spierings, A.B., Dawson, K., Voegtlin, M., Palm, F., Uggowitzer, P.J., 2016. Microstructure and mechanical properties of as-processed scandium-modified aluminium using selective laser melting. CIRP

Ann-Manuf. Technol. 65, 213-216.

Ungar, T., Borbely, A., 1996. The effect of dislocation contrast on x-ray line broadening: A new approach to line profile analysis. Appl. Phys. Lett. 69, 3173-3175.

Ungar, T., Dragomir, I., Revesz, A., Borbely, A., 1999. The contrast factors of dislocations in cubic crystals: the dislocation model of strain anisotropy in practice. J. Appl. Crystallogr. 32, 992-1002.

Wagner, J.N., Hofmann, M., Wimpory, R., Krempaszky, C., Stockinger, M., 2014. Microstructure and temperature dependence of intergranular strains on diffractometric macroscopic residual stress analysis. Mater. Sci. Eng. A 618, 271-279.

Wang, Y.M., Voisin, T., McKeown, J.T., Ye, J., Calta, N.P., Li, Z., Zeng, Z., Zhang, Y., Chen, W., Roehling, T.T., Ott, R.T., Santala, M.K., Depond, P.J., Matthews, M.J., Hamza, A.V., Zhu, T., 2018. Additively manufactured hierarchical stainless steels with high strength and ductility. Nat. Mater. 17, 63-71.

Wang, Z.H., Lin, X., Kang, N., Wang, Y.F., Yu, X.B., Tan, H., Yang, H.O., Huang, W.D., 2021a. Making selective-laser-melted high-strength Al-Mg-Sc-Zr alloy tough via ultrafine and heterogeneous microstructure. Scr. Mater. 203, 114052.

Wang, Z.H., Lin, X., Tang, Y., Kang, N., Gao, X.H., Shi, S.Q., Huang, W.D., 2021b. Laser-based directed energy deposition of novel Sc/Zr-modified Al-Mg alloys: columnar-to-equiaxed transition and aging hardening behavior. J. Mater. Sci. Technol. 69, 168-179.

Wei, D.X., Gong, W., Tsuru, T., Kawasaki, T., Harjo, S., Cai, B., Liaw, P.K., Kato, H., 2022. Mechanical behaviors of equiatomic and near-equiatomic face-centered-cubic phase high-entropy alloys probed using in situ neutron diffraction. Int. J. Plast. 158, 103417.

Wong, S.L., Madivala, M., Prahl, U., Roters, F., Raabe, D., 2016. A crystal plasticity model for twinning- and transformation-induced plasticity. Acta Mater. 118, 140-151.

Xie, Q.G., Lian, J.H., Sidor, J.J., Sun, F.W., Yan, X.C., Chen, C.Y., Liu, T.K., Chen, W.J., Yang, P., An, K., Wang, Y.D., 2020. Crystallographic orientation and spatially resolved damage in a dispersion-hardened Al alloy. Acta Mater. 193, 138-150.

Zecevic, M., Pantleon, W., Lebensohn, R.A., McCabe, R.J., Knezevic, M., 2017. Predicting intragranular misorientation distributions in polycrystalline metals using the viscoplastic self-consistent formulation. Acta Mater. 140, 398-410.

Zhang, X.X., Knoop, D., Andrä, H., Harjo, S., Kawasaki, T., Lutz, A., Lahres, M., 2021a. Multiscale constitutive modeling of additively manufactured Al-Si-Mg alloys based on measured phase stresses and dislocation density. Int. J. Plast. 140, 102972.

Zhang, X.X., Lutz, A., Andrä, H., Lahres, M., Gan, W.M., Maawad, E., Emmelmann, C., 2021b. Evolution of microscopic strains, stresses, and dislocation density during in-situ tensile loading of additively manufactured AlSi10Mg alloy. Int. J. Plast. 139, 102946.

Zhang, X.X., Lutz, A., Andra, H., Lahres, M., Sittig, D., Maawad, E., Gan, W.M., Knoop, D., 2021c. An additively manufactured and direct-aged AlSi3.5Mg2.5 alloy with superior strength and ductility: micromechanical mechanisms. Int. J. Plast. 146, 103083.

Zhang, Y., Ding, K.Q., Gu, Y.J., Chen, W., Wang, Y.M., El-Awady, J., McDowell, D.L., Zhu, T., 2022. Modeling of microscale internal stresses in additively manufactured stainless steel. Modell. Simul. Mater. Sci. Eng. 30, 074001.

Zhang, Y., Liu, J.P., Chen, S.Y., Xie, X., Liaw, P.K., Dahmen, K.A., Qiao, J.W., Wang, Y.L., 2017. Serration and noise behaviors in materials. Prog. Mater Sci. 90, 358-460.

Zhu, Y.T., Wu, X.L., 2023. Heterostructured materials. Prog. Mater Sci. 131, 101019.